

**Growth, Characterization, and Properties of Co/Re
Superlattices**

Timothy R. Charlton

Dissertation submitted to the
Eberly College of Arts and Sciences
at West Virginia University
in partial fulfillment of the requirements
for the degree of

Doctor of Philosophy
in
Physics

David Lederman
Nancy Giles
Larry Halliburton
Larry Hornak
Mohindar Seehra

Department of Physics

Morgantown, West Virginia
2001

Keywords: cobalt, rhenium, superlattice, giant magnetoresistance, thin films, neutron
reflectivity, magnetic spin-flop transition.

Copyright 2001 Timothy R. Charlton

ABSTRACT

Growth, Characterization, and Properties of Co/Re Superlattices

Timothy R. Charlton

All conducting materials have a magnetoresistive response (MR). In bulk ferromagnets the MR is due to the anisotropic magnetoresistance (AMR). AMR results from the spin-orbit interaction and s-d electron scattering. The change in resistance due to AMR is only a few percent. In contrast, the giant magnetoresistance (GMR) can be over 100%. The primary mechanism responsible for GMR is spin-dependent scattering. But where does this scattering occur? Some experiments show that the magnitude of the GMR depends on the thickness of the ferromagnetic layer, concluding that the scattering occurs in the bulk of the ferromagnet. Other studies that vary the interface roughness and composition conclude that the interface scattering is important.

To study this problem, we chose to investigate Co/Re superlattices. These superlattices are hcp with the c -axis, the magnetic easy axis, in the film plane, and have GMR and AMR contributions of comparable size. The basic idea is to use the AMR, as a probe to determine whether the scattering responsible for GMR occurs primarily at the interface or inside the Co layers. To do this, neutron reflectivity was used to find the magnetization vector in adjacent layers of Co and the MR was measured as a function of temperature. We found that in some geometries the GMR behaves like the AMR. Here the scattering responsible for GMR occurs in the Co layer. In other geometries, the GMR and the AMR behave differently as a function of temperature, so interface scattering is more important. This demonstrates that a fundamental understanding of the GMR must take into account the direction of current flow and the band structure of the materials.

In addition to the expected in-plane anisotropy, we surprisingly observed an interface induced out-of-plane anisotropy. This type of anisotropy to our knowledge has never been measured in Co systems with an in-plane c -axis before.

Co/Re superlattices can be used to test theories on ideal bulk antiferromagnets. Other magnetic superlattices have already been used in this capacity. In this dissertation we tested a surface spin-flop theory using our superlattices and found excellent agreement between the theoretical predictions and the experimental results.

Dedication

To my family. Without their continual support and encouragement this work would not have been possible.

Acknowledgements

I would like to thank the committee members for their time and energy spent on this dissertation. I would also like to acknowledge Erie Morales and Hong Tao Shi for their help in the lab and many useful discussions. I thank Gian Felcher of Argonne National Lab for his guidance and effort which made the neutron reflectivity measurements a reality. I thank Larry Hornak, Kolin Brown and Jeremy Dawson for the use of the photolithography lab and instruction on the lithography techniques and equipment. I thank the machine shop personnel, Carl Webber, Dough Mathess, and Tom Milam for their instruction on the use of the shop equipment, speedy fabrication time and design suggestions. Finally I would like to acknowledge David Lederman, my advisor, for his direction and uncompromising demand for perfection.

Thank you all.

Contents

Chapter	
1	Introduction 1
2	Background 3
2.1	Brief History of Magnetism 3
2.2	Origins of Magnetism 3
2.3	Band Structure and Magnetism 4
2.4	Magnetotransport 5
2.4.1	Resistivity in a Bulk Ferromagnetic Metals 5
2.4.2	Spin-Dependent Scattering 7
2.5	Previous Work in the Field 9
2.6	Hysteresis Loops 11
2.6.1	Ferromagnetic Loops 11
2.6.2	Antiferromagnetic Loops 13
3	Experimental Techniques 16
3.1	Growth 16
3.1.1	Sputtering 16
3.1.2	Sample Growth 18
3.2	Structural Measurements 19
3.2.1	X-Ray Reflectivity 19

3.2.2	X-Ray Diffraction	26
3.2.3	Summary	31
3.3	Magnetic Measurements	31
3.3.1	Magneto-Optic Kerr Effect	31
3.3.2	Vibrating Sample Magnetometry	33
3.3.3	SQUID Magnetometry	33
3.3.4	Ferromagnetic Resonance	34
3.4	Neutron Reflectivity	37
3.5	Magnetotransport	38
4	Results	43
4.1	In-plane Magnetic Anisotropy	43
4.2	Surface Induced Magnetic Perpendicular Anisotropy	45
4.3	Surface Spin Flop Transition	50
4.4	Spin-Dependent Scattering	58
5	Conclusions	68
	Bibliography	69

Figures

Figure

2.1	The Bohr picture of the hydrogen atom. The electron is shown in blue and the electron velocity vector is in red.	4
2.2	Density of states diagram of ferromagnetic Ni [1].	6
2.3	Cross section of a GMR multilayer at $H = 0$ and $H = H_{sat}$. The spin up electrons are shown in green and the spin down electron are shown in red.	8
2.4	Calculated hysteresis loops at different θ in a uniaxial system. θ is the angle between H and the magnetic easy axis. [2]	12
2.5	M vs H calculated for a 15 and a 16 bilayer superlattice. The circles represent a magnetic layer and the red arrows indicate the direction of the magnetization. The blue bracket indicates a domain wall [3].	14
3.1	A schematic of a typical magnetron sputtering gun [4].	17
3.2	Temperature at the substrate as a function of heater set point. The result of the linear fit is $T_{sample} = 0.627 T_{set} + 52.82^{\circ}\text{C}$	18
3.3	Re buffer grown at various temperatures. The Re $(10\bar{1}0)$, (0002) , and $(10\bar{1}1)$ reflections are labeled.	20
3.4	Schematic of a sample cross section.	21

3.5	Roughness as a function of growth temperature. The roughnesses at each interface are $\sigma_{Air-Re}(\times)$, $\sigma_{Co-Re}(\bullet)$, $\sigma_{Re-Co}(\circ)$, $\sigma_{Co-Buffer}(\ast)$, $\sigma_{Buffer-Substrate}(+)$. The line is a guide to the eye.	22
3.6	Diagram of the x-ray setup. The path of the x-ray beam is shown in red.	22
3.7	Low angle x-ray fit for a Co/Re superlattice.	25
3.8	High angle $\theta - 2\theta$ aligned with the buffer.	26
3.9	High angle $\theta - 2\theta$ aligned with the superlattice.	27
3.10	High angle in-plane $\theta - 2\theta$ scan with \mathbf{q} along the $[11\bar{2}0]$ direction of the buffer layer and the superlattice. The substrate $(03\bar{3}0)$, buffer layer, and superlattice $(11\bar{2}0)$ peaks are labeled.	29
3.11	High angle ϕ scan obtained by rotating the sample about the growth direction with \mathbf{q} fixed along the superlattice $(11\bar{2}0)$	29
3.12	$d_{SL}(t_{Co} + t_{Re})/t_{Co}$ plotted as a function of t_{Re}/t_{Co} , using the values of t_{Co} and t_{Re} obtained from low angle x-ray reflectivity fits. The blue line is a fit to the data for $t_{Re}/t_{Co} < 1.2$, yielded $d_{Co} = 2.13 \text{ \AA}$ and $d_{Re} = 2.46 \text{ \AA}$. The green line is a guide to the eye.	30
3.13	A block diagram of the MOKE setup.	32
3.14	Resonant line position as a function angle for a superlattice with $t_{Co} = 20 \text{ \AA}$ $t_{Re} = 6 \text{ \AA}$	35
3.15	Saturation magnetization measured by SQUID(\bullet) magnetometry and the effective magnetization (\circ) from the FMR experiment. All samples have $t_{Co} \sim 20 \text{ \AA}$. The line is a guide to the eye.	36
3.16	The POSY and POSY II instruments. POSY is shown the upper beam path, while POSY II is the lower beam path. All measurements were performed on POSY.	39
3.17	Typical neutron reflectivity scan over a q range up to the antiferromagnetic peak (at $q_z \sim 0.065$).	40

3.18	Contact geometries	40
3.19	Photograph of a sample patterned with photolithography. The direction of the c -axis is marked by the arrow. The gold wire bonds can be seen.	42
4.1	Hysteresis loops measured at room temperature for two different samples with $t_{Co} \sim 20 \text{ \AA}$ and $t_{Re} = 14.6 \text{ \AA}$ and $t_{Re} = 7.9 \text{ \AA}$ with H applied parallel and perpendicular to the c -axis.	44
4.2	The anisotropy constants K_1 (a) and K_2 (b) as a function of Re thickness. All samples have a $t_{Co} \sim 20 \text{ \AA}$. The lines are guides to the eye.	46
4.3	MOKE hysteresis loops measured with $H \parallel c$. Each loop is labeled by the Re layer thickness. All samples have a $t_{Co} \sim 20 \text{ \AA}$	47
4.4	(a) Three hysteresis loops a $H \parallel c$, $H 45^\circ c$, and $H \perp c$. (b) M_r and (c) H_c as function of angle between H and c for a $t_{Co} = 21 \text{ \AA}$ and $t_{Re} = 15 \text{ \AA}$ superlattice.	48
4.5	M_{sat} as a function of $1/t_{Co}$	49
4.6	Anisotropy constants as a function of $1/t_{eff}$. The points are the actual data and the line is a linear fit. K_{U1} (blue), K_{U2} (green), and K (red) are shown.	51
4.7	Angle between M_{AF} and c as a function of H . The \bullet are measured with $H \parallel c$ and \circ are measured with $H \perp c$	53
4.8	$M_{AF\perp}(\bullet)$, $M_{AF\parallel}(\circ)$, and $M_F(\triangle)$ obtained from neutron diffraction with spin polarization analysis.	54
4.9	Schematic of the magnetization in adjacent layers of Co.	55
4.10	MOKE hysteresis loops for a superlattice with (a) 20 bilayers and (b) 21 bilayers. Color coding and arrows denote the sweep direction. (c) SQUID and MOKE magnetization curves from $+H_{sat}$ to $-H_{sat}$	56

4.11 Hysteresis loops measured by MOKE and SQUID (a) and the resistivity (b) with $H \parallel c$ and $H \parallel I$ at $T = 300$ K.	59
4.12 The magnetoresistance as a function of magnetic field at $T = 5$ K (red) and $T = 250$ K (blue) for four separate geometries. The data were obtained measuring from positive to negative and negative to positive fields. The difference in the values at high positive fields are due to small differences in the temperature.	61
4.13 Magnetoresistance measurements (blue) and simulation (red) at $T = 5$ K. The simulation qualitatively matches the data.	62
4.14 Simulation broken down into total MR (blue), AMR (green) and GMR (red) contributions.	64
4.15 Magnitude of the AMR and the GMR plotted as a function of temperature.	65
4.16 The magnitude of GMR/AMR plotted as a function of temperature. . . .	66
4.17 Resistivity as a function of temperature at $H = 0$	67

Chapter 1

Introduction

Magnetic thin films have been of great interest of late due to their technological application in magnetic sensors and magnetic random access memory (MRAM) modules. In superlattices and multilayers there is an abundance of interesting phenomena to study relevant to magnetic thin films. Multilayers are artificially grown stacked layers, while superlattices are multilayers with lateral structural / crystallographic coherence. Giant magnetoresistance, the effect upon which all recent computer hard drives use to sense data bits, was discovered in Fe/Cr multilayers in the late 1980's. Whenever the magnetoresistance is measured in a ferromagnet, the anisotropic magnetoresistance, studied extensively in the 1930's in bulk ferromagnets, must be considered. Only recently have both effects been studied in the same system, including studies of Co/Cr [5], Fe/Cr [6], Co/Ru [7], and Co/Cu [8] multilayers. Other recent experiments on Co/Cr multilayers [5] focus on using AMR to enhance the total magnetoresistance of a GMR system with a magnetocrystalline anisotropy. One of the most important questions raised by the above investigations deals with determining the nature of the scattering mechanism responsible for GMR.

There are several other interesting aspects to magnetic thin films than just GMR. Novel magnetic alignments like magnetic exchange springs [9] are being investigated not only for their academic interest, but also for their use in microdevices. Recently, 90° alignment of the magnetization in alternating Fe layers in Fe/Cr superlattices were

observed [10]. Both periodic and aperiodic oscillations in the coupling strength between the ferromagnetic layers separated by a nonmagnetic spacer have been reported in systems like Fe/Cr [6, 11] and Co/Ir [12, 13, 14].

Magnetic multilayers also prove to be a model system for investigating the magnetization reversal process in antiferromagnets. In 1967 D. L. Mills [15] proposed a theory for a surface spin-flop (SSF) transition in an ideal antiferromagnet. The SSF in a bulk system is a sudden flop of the antiferromagnetic moments at the surface from pointing along the anisotropy axis, parallel to the applied magnetic field (H), to nearly perpendicular to H . The SSF, according to the theory, only occurs when the direction of the top surface magnetization is antiparallel to the bottom surface magnetization. Otherwise only the bulk spin-flop transition is realized. Physically this can only happen when the number of magnetic layers is even. Measuring the SSF in a real bulk antiferromagnet however is next to impossible. Any atomic disorder at the surface will give rise to a mixture of odd and even number of magnetic planes. Only relatively recently have the theories been tested experimentally in Fe/Cr [3], and now in Co/Re superlattices (see section 4.3), where atomic disorder has little effect on the overall magnetic alignment of a layer.

Chapter 2

Background

2.1 Brief History of Magnetism

The first known magnetic material, magnetite (sometimes called lodestone), was discovered in China in 6th century BC. The word magnetism originated from the name of the city Magnesia in Asia Minor, where deposits of magnetite ore can still be found. Several Greek natural philosophers such as Thales, Epicurus and Democritus noted the interesting properties of magnets and in their writing tried to explain them. A Roman scientist named Lucretius Carus described a stone magnet moving iron filings and rings in the poem "On the Nature of Things" [16].

Magnetism was well known in antiquity and throughout the middle ages where magnetic properties were attributed to spiritual forces. During the Renaissance, Rene Descartes presented the first materials theory of magnetism [16]. But it wasn't until the 1900's, with the advent of quantum mechanics, that the origins of magnetism were finally understood.

2.2 Origins of Magnetism

Starting from the Bohr model of the atom the magnetic moment of an atom or ion can be derived from classical physics. Figure 2.1 shows the Bohr picture of the hydrogen atom, which is modeled as a small current loop with current $I = ev/2\pi r$. The loop's magnetic dipole moment can be written as $\mu = I\pi r^2$ or $\mu = (e/2m)L$, where $L =$

mvr is the angular momentum of the electron. From quantum mechanics, it is known that the electron has spin angular momentum, $S = \pm\hbar/2$, with a magnetic moment of $\mu_B = e/2mS$. The total magnetic moment of an electron is $\mu = |J|e/2m$ where $\vec{J} = \vec{S} + \vec{L}$.

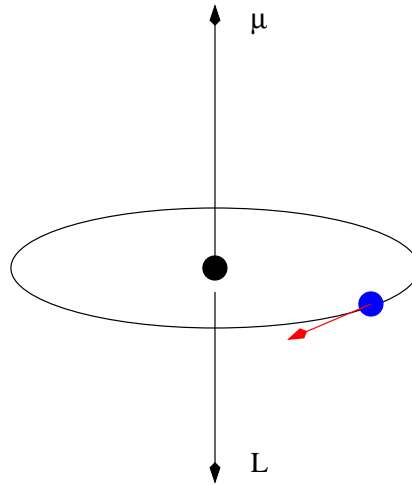


Figure 2.1: The Bohr picture of the hydrogen atom. The electron is shown in blue and the electron velocity vector is in red.

Armed with the magnetic moment due to the electron, we can calculate the magnetic moment for any atom or ion given its electron configuration, J . This simple description of the magnetic moment [17] works well for the rare earth elements because the f -electrons are well-localized, but fails for the iron group elements. For the iron group we must consider the crystal field, due to the arrangement of the atoms in a periodic lattice, which leads to a dramatic decrease in time-averaged orbital angular momentum, known as orbital quenching [18].

2.3 Band Structure and Magnetism

Almost all materials properties are influenced by the structural arrangement of the atoms or ions in the material and their effects on the electron wave function. Op-

tical properties and electrical and thermal conductivity are good examples of this. By solving Schrodinger's equation in a solid, we find that electrons exist in groups of allowed energies known as energy bands. The energy bands are separated by regions of forbidden energies known as band gaps [18].

Insulators have a Fermi energy (E_F), half way between the highest occupied electron energy state and the lowest unoccupied state, lying in an energy gap for semiconductors and insulators, while in metals E_f lies in the conduction energy band. Good conducting noble metals like Cu, Ag and Au have a partially filled s -shell and completely filled d -shells. In these metals, the s -electrons are primarily responsible for conduction because the d -electron- like bands lie well below the E_F .

2.4 Magnetotransport

2.4.1 Resistivity in a Bulk Ferromagnetic Metals

In ferromagnetic metals such as Fe, Co and Ni, the d bands participate in electrical conduction. In these metals, E_F lies near the d -electrons bands which, due to the semi-localized nature of these electrons, are relatively flat and thus have a high density of states. The high density of states at E_F results in a large scattering probability for s -like electrons, resulting in a high resistivity [1, 19, 20]. Understanding the resistivity is further complicated by the fact that the electrons have spin, which results in an effective exchange interaction between electrons due to the Pauli exclusion principle. In Fe, Ni and Co the exchange interaction, together with the high density of states at E_F , results in energy bands split into a spin-up and spin-down bands, shown in figure 2.2, and thus a spontaneous magnetic moment. The traditional way of dealing with the two possible spin states is to consider their contributions separately. This is called the parallel resistor model.

Ferromagnetic transition metals also show a dependence of the resistance on the

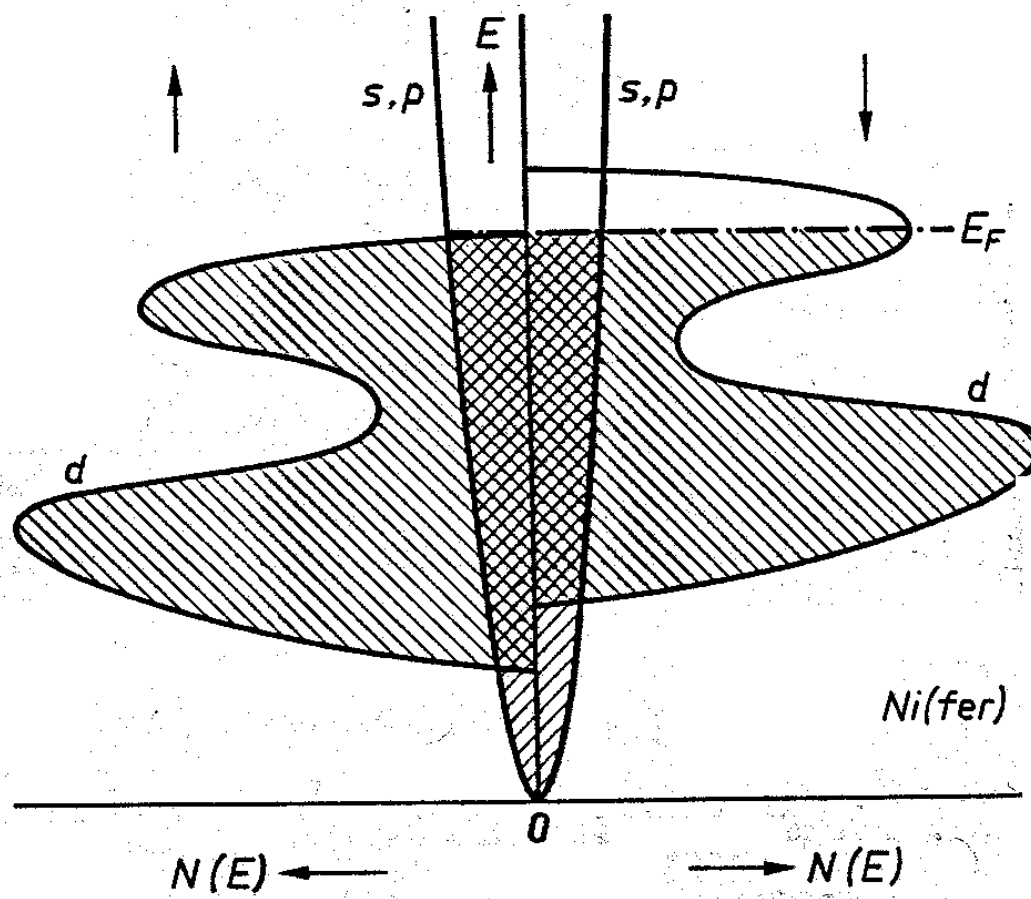


Figure 2.2: Density of states diagram of ferromagnetic Ni [1].

angle between the sensing current and the magnetization direction. This dependence in a macroscopic bar-shaped sample is given by

$$\rho(H) = \frac{1}{3}\rho_{\parallel} \cos^2 \gamma + \frac{2}{3}\rho_{\perp} \sin^2 \gamma, \quad (2.1)$$

where γ is the angle between \vec{I} and \vec{M} , $\rho_{\parallel(\perp)}$ is the resistivity with $\vec{M} \parallel (\perp) \vec{I}$, and \vec{I} is the current. This effect is known as anisotropic magnetoresistance (AMR). Studied since the 1930's [2] in bulk ferromagnets and alloys, the overall size of AMR is a few percent when measuring $\Delta\rho/\rho_{sat}$, where $\Delta\rho = \rho(H) - \rho_{sat}$ and ρ_{sat} is the resistivity at saturation. This is sufficient for magnetic detectors [21] but is crude by today's standards. Spin-orbit coupling indirectly couples the electron spin to the lattice structure through the crystal field. The coupling mixes the spin-up and spin-down states in the electron wavefunction as one would expect from perturbation theory. When calculating the matrix elements for $s-d$ scattering, Smit [22] noticed that for $I \perp M$ the spin-down electrons have a smaller scattering probability than for $I \parallel M$. This leads directly to the result $\rho_{\parallel} > \rho_{\perp}$, which is observed in the bulk ferromagnets [19]. The more complete theoretical description of angular dependence, however is not straightforward [19]. Although the magnetization dependence on the resistivity is complicated, the main mechanism responsible for AMR is anisotropic $s-d$ scattering [23].

2.4.2 Spin-Dependent Scattering

Giant magnetoresistance (GMR) was discovered in antiferromagnetically-coupled Fe/Cr multilayers in the late 1980's [24]. GMR can be greater than 100% at room temperature. The existence of GMR in a multilayer relies on two conditions. First, at least two magnetic layers separated by a non-magnetic layer must be present, and second, adjacent ferromagnetic layers must be antiferromagnetically (AF) aligned at zero applied field. The AF alignment is a direct result of the RKKY interaction through the non-magnetic metal [25].

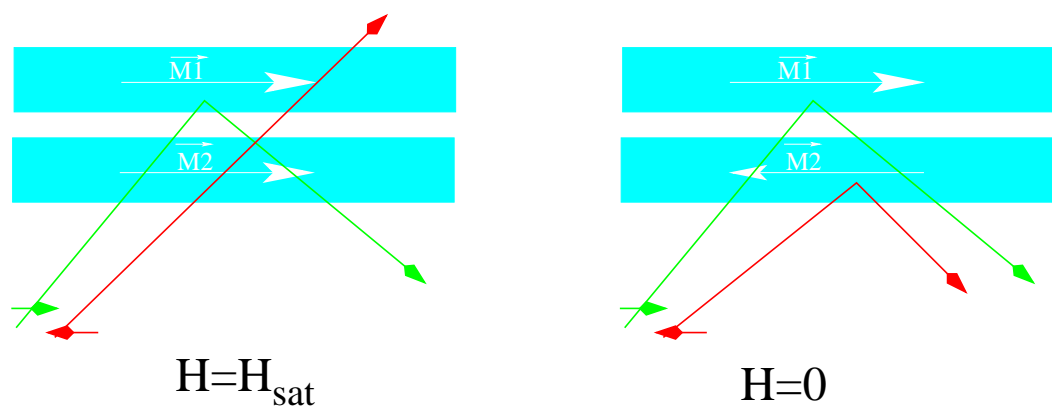


Figure 2.3: Cross section of a GMR multilayer at $H = 0$ and $H = H_{sat}$. The spin up electrons are shown in green and the spin down electrons are shown in red.

The GMR arises from spin-dependent scattering either in the magnetic layer or at the magnetic/non-magnetic interface. Figure 2.3 shows a GMR multilayer at saturation and zero applied field. At $H = 0$ both the spin up (green) and spin down (red) electrons are scattered strongly but, at $H = H_{sat}$, when the magnetizations are parallel, one spin state (in the figure the red spin down electron) is scattered much less than the other, causing a large drop in the resistance. This mechanism relies on the fact that the spin-flip crosssection is small, so that electrons tend to scatter into states matching their own spin.

2.5 Previous Work in the Field

Since the discovery of GMR in thin film Fe/Cr superlattices [24], many similar materials systems have also been studied. From these investigations researchers have found other interesting effects such as oscillatory exchange coupling, novel 90° magnetic alignments [10], and enhancements to the GMR by AMR. This section describes the similarities between Co/Re superlattices and other superlattice systems.

Oscillatory exchange coupling has been observed in many superlattice systems such as Co/Ir [14], Fe/Cr [6, 11], Co/Cu [26] and Co/Ru [26]. This effect is seen in the oscillations of the saturation magnetization and the magnitude of the magnetoresistance as functions of the nonmagnetic layer thickness. Similar to the RKKY interaction found in bulk systems with magnetic impurities [18], the magnetization of adjacent magnetic layers align parallel, antiparallel, or perpendicular to each other depending on the non-magnetic layer thickness.

Relatively recently, there have been several studies concerned with the nature of the scattering mechanism responsible for GMR. In Fe/Cr superlattices grown via sputtering, varying the amount and type of interface roughness leads to the conclusion that the GMR increases with increasing roughness [27]. In another attempt to study the importance of the interface, simpler Py/Cu/Py (Py = permalloy = $\text{Ni}_{81}\text{Fe}_{19}$) spin

valves structures (trilayer films) were studied [28]. Several spin valves were grown with increasing thickness of Co at the Py-Cu interfaces. As the Co thickness increases, the magnitude of the GMR increases as well. To further determine the relative importance of the interface over the bulk of the ferromagnetic layer, several spin valves with a 5 Å layer of Co at varying distances from the Cu layer were grown. The GMR decreases as the Co layer is moved away from the Py-Cu interface [28]. Similar studies of *c*-axis textured Co/Re superlattices showed a similar dependence [29].

If these were the only investigations concerning this matter, it would be easy to conclude that GMR is solely an interface effect, that is, spin-dependent scattering occurs at the interface. Investigations of Ni₈₀Fe₂₀/Cu/Ni₈₀Fe₂₀ multilayers with a varying Ni₈₀Fe₂₀ thickness, however, show that the GMR has a clear FM layer thickness dependence [30]. Also, a complete study of the GMR of several polycrystalline spin valve systems with different FM materials, demonstrate a universal relationship between the AMR and the GMR [31]. These studies conclude that the bulk properties of the FM layer are important to GMR.

Taken as a whole, these investigations are inconclusive unless both are somehow correct. To sort this out, Co/Re epitaxial superlattices were studied in this dissertation for several reasons. The materials were readily available and it is relatively easy to grow epitaxially on sapphire substrates. Co/Re has AMR and GMR contributions of comparable size and can be modeled empirically once the magnetic configuration as a function of magnetic field is determined. If the temperature dependence of the AMR and GMR are different, then the GMR is a surface effect because the spin-dependent scattering mechanism must be different.

Previous studies of Co/Re were performed on polycrystalline or *c*-axis textured samples [32]. Measurements of magnetization and MR showed no evidence of oscillatory exchange coupling [29]. The largest MR reported in this system did not exceed 2% at 18 K [32].

2.6 Hysteresis Loops

2.6.1 Ferromagnetic Loops

One of the earlier interesting discoveries about ferromagnets is the hysteresis when measuring the magnetization as a function of the applied field, H . Theoretically it is known that hysteresis originates from irreversible magnetization processes [33]. These irreversible processes include domain wall motion, domain nucleation, and magnetization rotation processes. Each process has a unique signature in the M-H loop.

Any bulk or thin film ferromagnet can have magnetic domains, regions where the magnetization points along different directions, separated by domain walls. At saturation (H_{sat}), the entire sample is essentially a single domain with its magnetization pointing parallel to the external field. As the external field sweeps to $-H_{sat}$, at some point it becomes energetically favorable for domains to form because this decreases the total magnetic energy of the sample. The total magnetization of the sample decreases in a series of jumps called Barkhausen jumps. These jumps are caused by the sudden motion of domain walls which stop at defects in the sample. Figure 2.4 shows Chikazumi's calculated M-H hysteresis loops at various angles (θ) between H and the magnetic easy axis [2]. A magnetic easy axis is an axis or direction in which the energy is a minimum when the magnetization points in that direction [18]. To calculate the hysteresis loops, the local minimum in the energy density with respect to ϕ , the angle between the magnetization (M) and the easy axis, must be found. The energy density can be written as

$$E(\theta, \phi) = MH \cos(\phi - \theta) + K_{U1} \sin^2 \phi + K_{U2} \sin^4 \phi + 4\pi MH. \quad (2.2)$$

Terms on the right hand side of equation 2.2 include the Zeeman energy, uniaxial anisotropy and shape anisotropy for an infinite thin slab. There is no energy term in equation 2.2 for domain wall pinning due to defects, but the effect is included in the

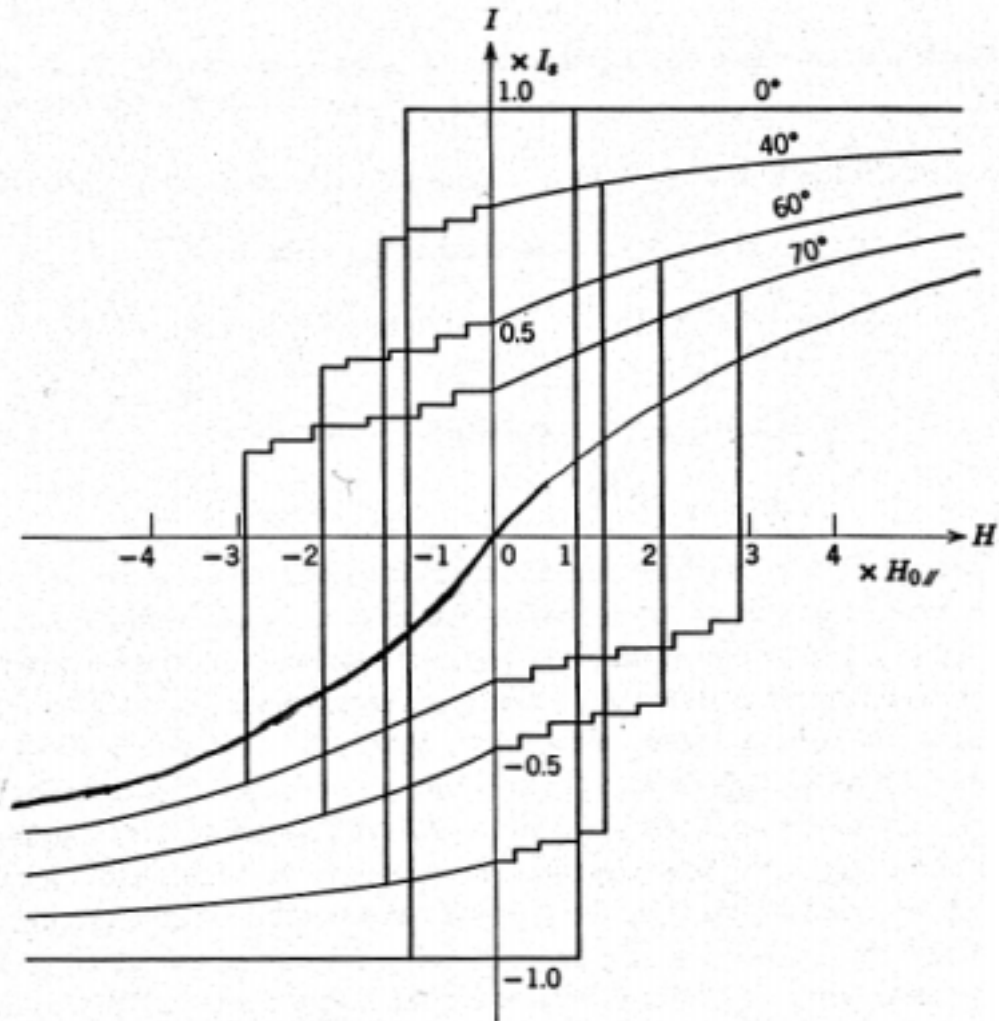


Figure 2.4: Calculated hysteresis loops at different θ in a uniaxial system. θ is the angle between H and the magnetic easy axis. [2]

figure. The calculations shown in figure 2.4 include reversible rotation and irreversible domain wall motion. Notice that for loops labeled 40° , 60° , 70° , as the external field is brought from positive saturation to zero, the curve is smooth. This is a typical feature of reversible rotation. The steps in the loop after H crosses the y-axis are Barkhausen jumps caused by the domain wall being pinned at a defect in the sample. It is also useful to note the remanent magnetization (M_r) and the coercive field (H_c) dependence on angle. The M_r is a maximum at 0° and decreases smoothly to $M_r = 0$ for the hard direction. The H_c , on the other hand, increases from 0° to a maximum somewhere between 0° and 90° , but at 90° H_c drops suddenly to zero. This angular dependence is experimentally observed in Co/Re superlattices, as shown in section 4.2.

2.6.2 Antiferromagnetic Loops

The interest in the nature of the magnetization reversal in an antiferromagnet extends back to Néel [34] theoretically and Poulis and Hardeman [35] experimentally. They both showed that when an external field is applied along the easy-axis, the antiferromagnet undergoes a first order phase transition known as a spin-flop transition. Spin-flop refers to the abrupt rotation of the antiferromagnetic moment 90° to the easy axis, causing a jump in the magnetization [36]. In a finite system, the spin-flop (SF) transition starts at the surface since it is only exchange-coupled on one side to the bulk, and propagates inward evolving into the bulk spin-flop transition. In bulk systems, the critical field at the bulk spin-flop transition is given by $H_B^2 = 2H_E H_A - H_A^2$, where $H_A = K/M$ is the anisotropy field, $H_E = J/M$ is the exchange field, and J is the exchange constant. A detailed theoretical description, and experimental confirmation of the theory, of the evolution of the surface SF into the bulk SF has been presented using antiferromagnetically coupled Fe/Cr superlattices [3]. Figure 2.5 shows the calculation by Wang and Mills for a 15 and a 16 bilayer superlattice with $J \ll K$. At $H = 0$ the system is aligned antiferromagnetically. As H is increased, the surface flops first for the

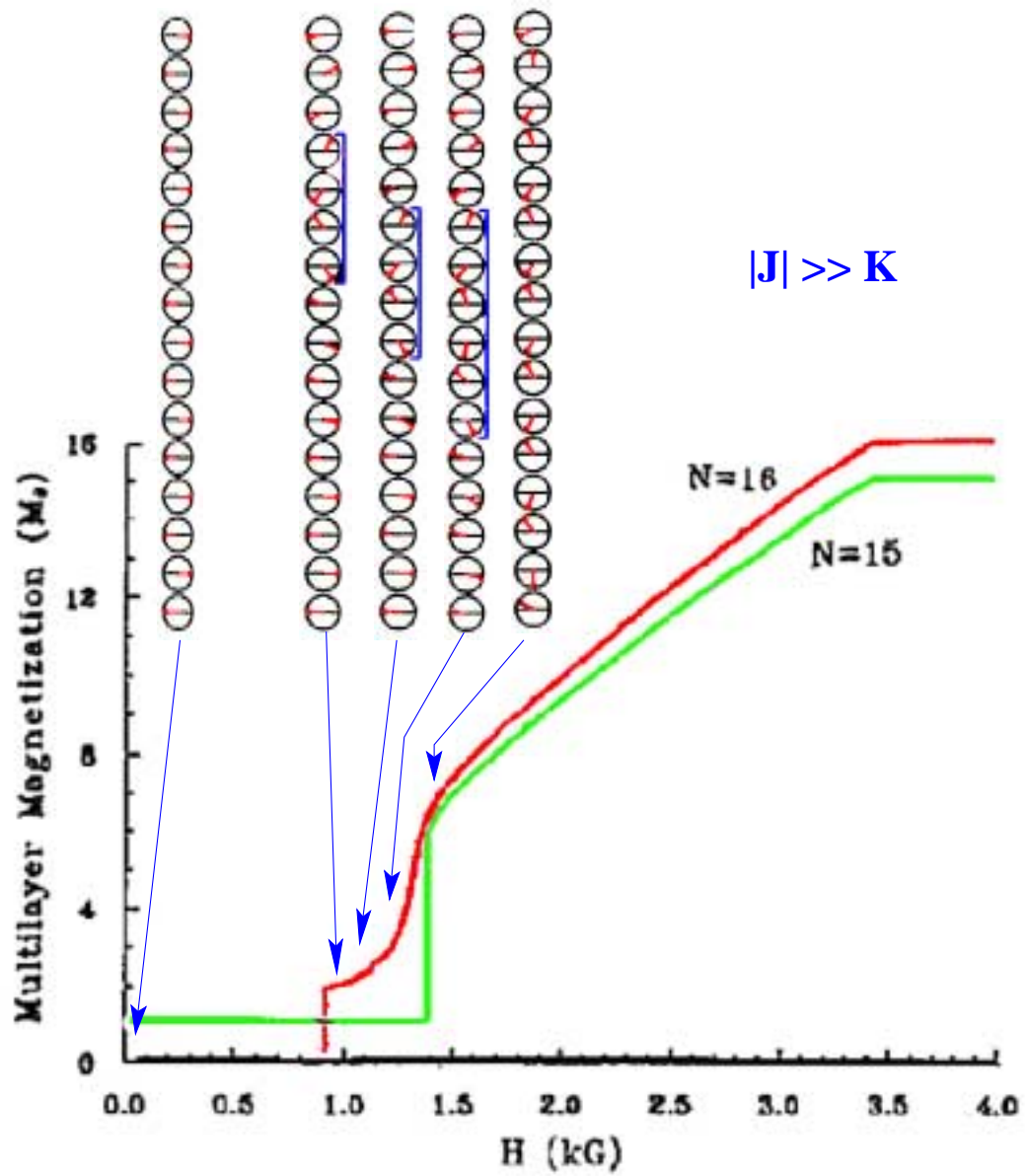


Figure 2.5: M vs H calculated for a 15 and a 16 bilayer superlattice. The circles represent a magnetic layer and the red arrows indicate the direction of the magnetization. The blue bracket indicates a domain wall [3].

16 bilayer sample. Afterwards a domain wall is formed, and as H increases further, it moves toward the center of the sample in a series of jumps. Once at the center, the wall increases in size until it encompasses all of the film layers. This is the bulk spin-flop field, H_B , roughly a factor of $\sqrt{2}$ higher than the surface spin-flop field, H_{SSF} . H_{SSF} is defined as $H_{SSF}^2 = H_E H_A - H_A^2$. Notice that the superlattice with an odd number of bilayers only shows signs of the bulk spin flop transition as expected. The experimental data for Fe/Cr superlattices [3, 37] strongly support the theory. Similar evidence supporting this description is also found in Co/Re superlattices and discussed in section 4.3.

Chapter 3

Experimental Techniques

3.1 Growth

3.1.1 Sputtering

Our samples were grown via magnetron sputtering. While lacking the total control and ultra-clean environment of molecular beam epitaxy (MBE), sputtering offers shorter growth times. Argon makes a good choice for the sputtering gas due to its low ionization potential and relatively heavy ions. The weight of the ion is important because sputtering is like sand blasting: the target material is knocked off the target by exchanging momentum with the colliding argon ion.

Figure 3.1 shows a diagram of a sputtering source, sometimes called a gun. The target is held at a large negative voltage which accelerates argon ions into the target. When the argon is ionized, some of the electrons are trapped by the magnetic field set up by the gun. Any argon atom entering the region of the electron cloud has a greater chance of being ionized. Once ionized the ions bombard the target cathode blasting off target material. This increases the efficiency of the gun, lowers the sputtering pressure, and increases the possible growth rates.

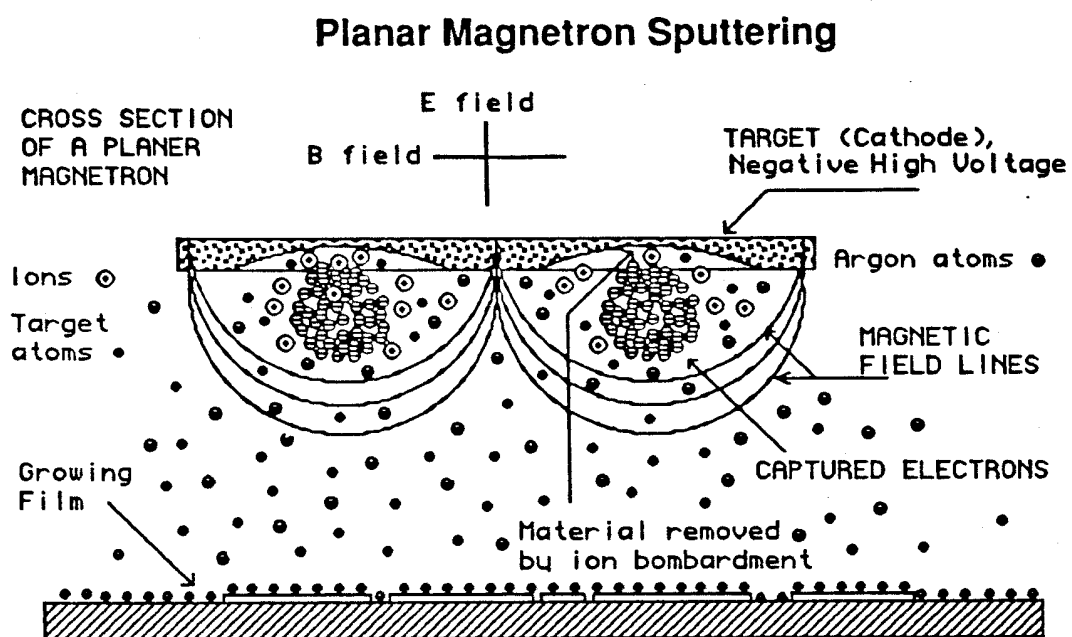


Figure 3.1: A schematic of a typical magnetron sputtering gun [4].

3.1.2 Sample Growth

Samples were grown in high vacuum by dc magnetron sputtering with a base pressure of 3.0×10^{-7} Torr. The system contains four sputtering guns focused on the substrate, each with its own crystal thickness monitor and shutter. All shutters are controlled by a crystal monitor controller. Up to five substrates may be loaded at one time. A quartz lamp heater can heat the substrate to a temperature 575°C . The temperature was calibrated (see figure 3.2) by placing a thermocouple on the surface of a Al_2O_3 substrate and adjusting the power to the heater.

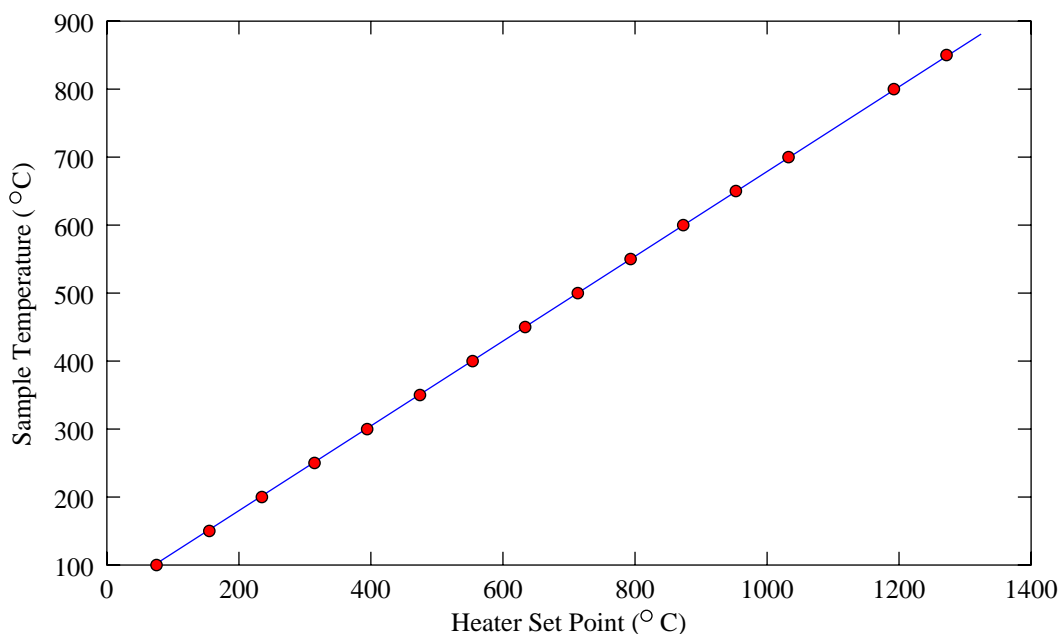


Figure 3.2: Temperature at the substrate as a function of heater set point. The result of the linear fit is $T_{sample} = 0.627 T_{set} + 52.82^\circ\text{C}$.

The Al_2O_3 substrates were prepared using a degreasing procedure and then etched in acid. The degrease consisted of rinsing the substrate in TCE for 5 min., acetone for 2 min., and finally methanol for 5 min., all at 70°C . The acid etch was a 3:1 mixture of phosphoric and sulfuric acids at 140°C for 10 min. This was followed by a deionized

H₂O rinse and blown dry with nitrogen. The substrate was then mounted in the vacuum system and outgassed at 575 °C for 30 min. in vacuum. The temperature was then lowered to 560 °C and a 50 Å Re buffer layer was deposited. The buffer layer growth temperature was chosen because the x-ray diffraction scans on single layer Re films showed smooth single crystal growth, as shown in figure 3.3. Next the superlattice was deposited at 150°C. A schematic of the sample's cross section is shown in figure 3.4.

To determine the optimum growth temperature for the superlattice, we studied the interface disorder in the bilayers of the superlattice using low angle x-ray reflectivity. A complete description of the low angle x-ray fitting will be given later in section 3.2.1. Interface roughnesses and layer thicknesses were obtained by fitting the true specular reflectivity to a dynamic model taking into account multiple reflections at each interface. Plotted in figure 3.5 is the interface roughness as a function of growth temperature. At high temperatures the roughness is mainly due to interdiffusion between the layers. At lower temperatures step disorder is more likely the cause for the increase in the roughness. We chose the temperature for the minimum roughness to be the growth temperature for the rest of the superlattices.

3.2 Structural Measurements

3.2.1 X-Ray Reflectivity

X-ray reflectivity experiments were carried out using Cu-K_α radiation from an 18 kW rotating anode source. The x-ray beam was focused at the center of a 29 cm two-circle, computer-controlled goniometer using a graphite bent crystal monochromator, collimated to a width of $\sim 0.02^\circ$. A block diagram of the x-ray experiment is shown in figure 3.6. Three types of scans were performed on the two-circle goniometer: a 2θ scan, a $\theta - 2\theta$ scan and a θ -scan, also known as a rocking curve. A 2θ scan is used primarily for alignment and observing the profile of the incident beam. To perform a

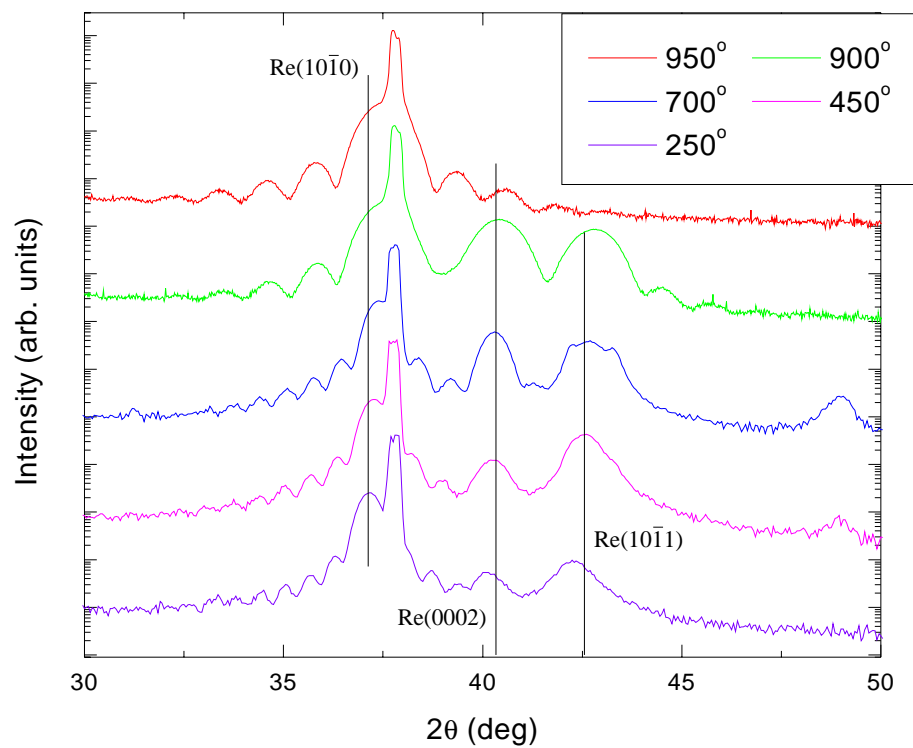


Figure 3.3: Re buffer grown at various temperatures. The Re $(10\bar{1}0)$, (0002) , and $(10\bar{1}1)$ reflections are labeled.

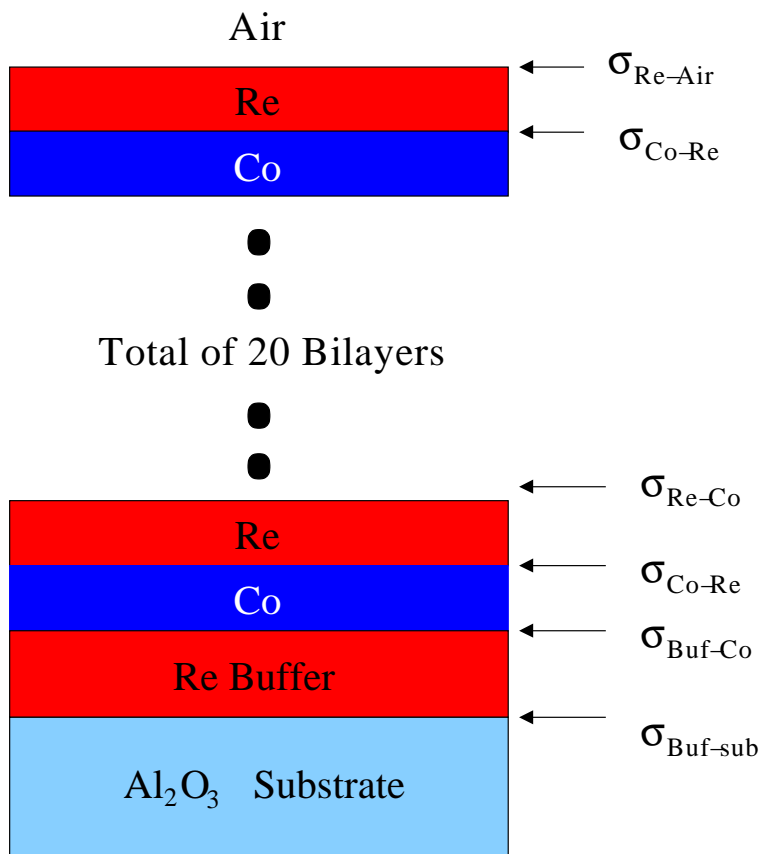


Figure 3.4: Schematic of a sample cross section.

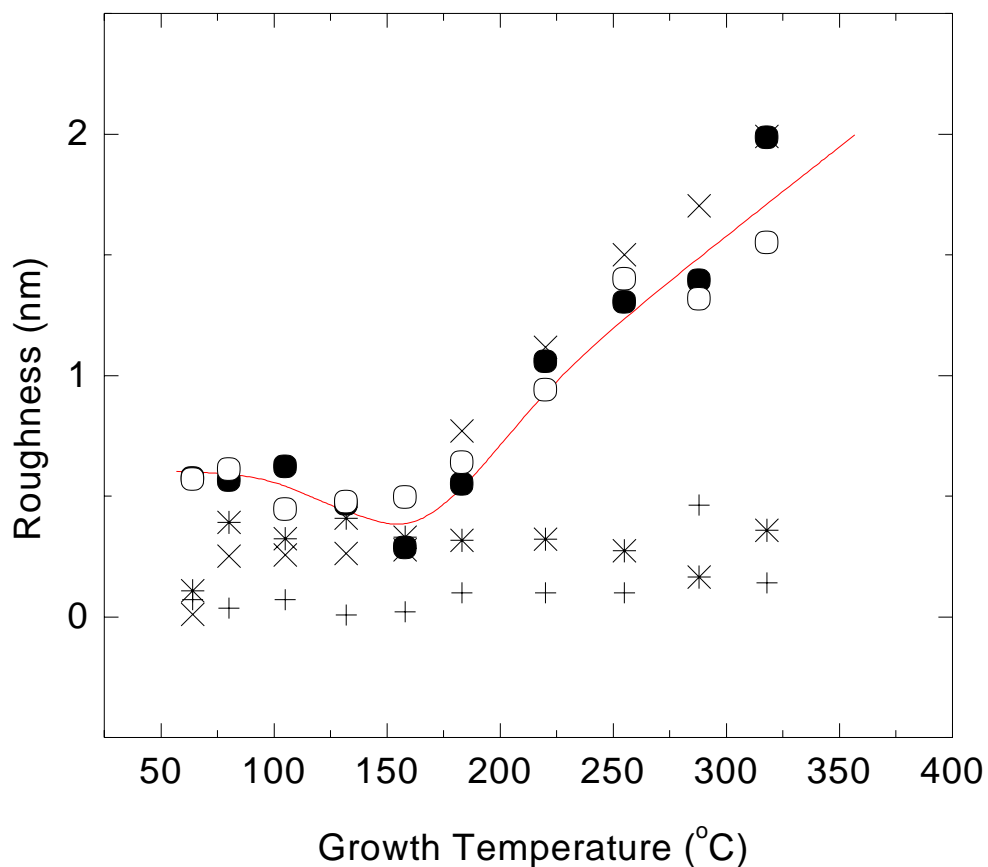


Figure 3.5: Roughness as a function of growth temperature. The roughnesses at each interface are $\sigma_{Air-Re}(\times)$, $\sigma_{Co-Re}(\bullet)$, $\sigma_{Re-Co}(\circ)$, $\sigma_{Co-Buffer}(\ast)$, $\sigma_{Buffer-Substrate}(+)$. The line is a guide to the eye.

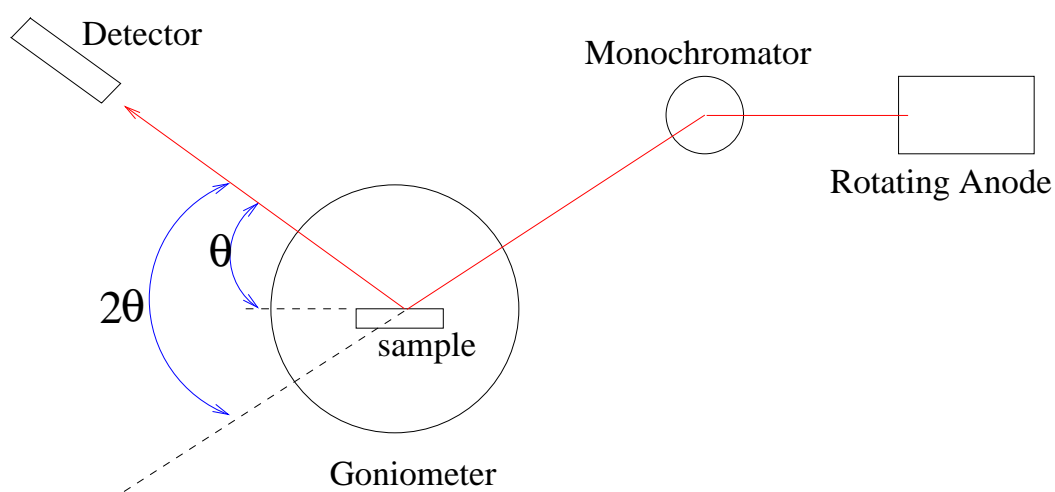


Figure 3.6: Diagram of the x-ray setup. The path of the x-ray beam is shown in red.

θ -scan, the detector (2θ) is placed at a Bragg condition, typically for the superlattice period, and the sample is rotated through an angle range around the specular condition. In a $\theta - 2\theta$ scan the angle of incidence and the angle of reflection are equal and scanned over an angle range to vary the momentum transfer vector perpendicular to the plane of the sample.

The true specular reflectivity [38] was measured by first performing a $\theta - 2\theta$ scan and then subtracting the background, determined by a $\theta - 2\theta$ scan with θ offset by $\sim 0.10^\circ$. The true specular reflectivity is then modeled [39] to obtain the layer thicknesses and interface roughnesses as described below.

The low-angle x-ray reflectivity pattern is calculated using an optical recursion matrix model [39]. Figure 3.4 shows the sample cross section. At any interface the electric field above the interface can be written as

$$E(x, y) = [A \exp(-ik_0 y \sqrt{n_{>}^2 - \sin^2 \theta}) + B \exp(ik_0 y \sqrt{n_{>}^2 - \sin^2 \theta})] \exp(ik_0 x \sin^2 \theta) \quad (3.1)$$

and below the interface as

$$E(x, y) = [C \exp(-ik_0 y \sqrt{n_{<}^2 - \sin^2 \theta}) + D \exp(ik_0 y \sqrt{n_{<}^2 - \sin^2 \theta})] \exp(ik_0 x \sin^2 \theta), \quad (3.2)$$

where $k_0 = 2\pi/\lambda$ with λ the wavelength of the incident x-rays, $n_{<(>)}$ is the index for x-rays below(above) the interface, x is the coordinate in the sample plane, y is the coordinate normal to the sample plane, θ is the angle of incidence, $A(B)$ is the magnitude of the electric field above the interface traveling in the $-y(y)$ direction, and similarly for $C(D)$ below the interface. Here the index of refraction for the x-rays is

$$n = 1 - \frac{\rho_N r_e \lambda^2}{2\pi} (f_0 + \Delta f' - i\Delta f''), \quad (3.3)$$

where ρ_N is the atomic density, r_e is the classical electron radius, f_0 is the atomic scattering power, and $\Delta f'$ and $\Delta f''$ are the anomalous dispersion corrections for the

atomic scattering power. At the boundary, the first derivatives of the electric field must be continuous. The matrix for the boundary conditions is written as

$$\begin{bmatrix} A \\ B \end{bmatrix} = \begin{bmatrix} p11 \exp(-\beta^2 \sigma^2 / 2) & p12 \exp(-\alpha^2 \sigma^2 / 2) \\ p21 \exp(-\alpha^2 \sigma^2 / 2) & p22 \exp(-\beta^2 \sigma^2 / 2) \end{bmatrix} \cdot \begin{bmatrix} C \\ D \end{bmatrix} \quad (3.4)$$

where

$$p11 = \left(1 + \frac{\sqrt{n_{>}^2 - \sin^2 \theta}}{\sqrt{n_{<}^2 - \sin^2 \theta}}\right) \exp[-iy(\sqrt{n_{<}^2 - \sin^2 \theta} - \sqrt{n_{>}^2 - \sin^2 \theta})],$$

$$p22 = \left(1 + \frac{\sqrt{n_{>}^2 - \sin^2 \theta}}{\sqrt{n_{<}^2 - \sin^2 \theta}}\right) \exp[-iy(\sqrt{n_{<}^2 - \sin^2 \theta} - \sqrt{n_{>}^2 - \sin^2 \theta})],$$

$$p12 = \left(1 - \frac{\sqrt{n_{>}^2 - \sin^2 \theta}}{\sqrt{n_{<}^2 - \sin^2 \theta}}\right) \exp[-iy(\sqrt{n_{<}^2 - \sin^2 \theta} + \sqrt{n_{>}^2 - \sin^2 \theta})],$$

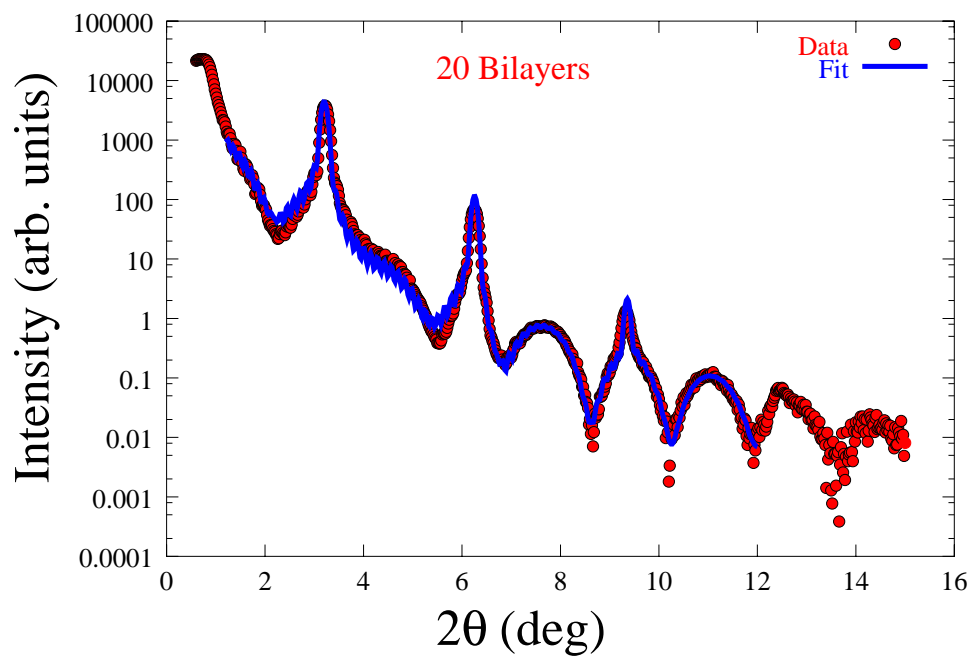
$$p21 = \left(1 - \frac{\sqrt{n_{>}^2 - \sin^2 \theta}}{\sqrt{n_{<}^2 - \sin^2 \theta}}\right) \exp[-iy(\sqrt{n_{<}^2 - \sin^2 \theta} + \sqrt{n_{>}^2 - \sin^2 \theta})],$$

$$\alpha = \sqrt{n_{<}^2 - \sin^2 \theta} - \sqrt{n_{>}^2 - \sin^2 \theta},$$

$$\beta = \sqrt{n_{<}^2 - \sin^2 \theta} + \sqrt{n_{>}^2 - \sin^2 \theta},$$

and σ is the layer roughness. To find the reflection matrix for the entire sample starting from the top, the layers' matrices are multiplied together. The model is then fit to the data using the Levenberg-Marquardt least-squares minimization routine from Numerical Recipes [40]. In order to enhance the important features at larger values of 2θ , the logarithm of the model is fit to the logarithm of the data.

Figure 3.7 shows two x-ray reflectivity scans with the lines corresponding to the numerical model and points representing the data. The interface roughness between the Co and Re layers is $\sigma \sim 4 \text{ \AA} \pm 2 \text{ \AA}$, where 2σ is the full width of the interface. The uncertainty of the fitting parameters was determined by fixing the parameter of interest and then fitting all other parameters, and recording the χ^2 as a function of the parameter of interest.



Fitting parameters

$t_{\text{Buf}} = 52.0 \pm 1 \text{ \AA}$	$t_{\text{Co}} = 20.5 \pm 1 \text{ \AA}$	$t_{\text{Re}} = 8.0 \pm 1 \text{ \AA}$
$\sigma_{\text{Buf-sub}} = 1.6 \pm 1 \text{ \AA}$	$\sigma_{\text{Co-Buf}} = 1.4 \pm 1 \text{ \AA}$	$\sigma_{\text{Re-Air}} = 3.6 \pm 1 \text{ \AA}$
$\sigma_{\text{Co-Re}} = 3.0 \pm 1 \text{ \AA}$	$\sigma_{\text{Re-Co}} = 4.4 \pm 1 \text{ \AA}$	

Figure 3.7: Low angle x-ray fit for a Co/Re superlattice.

3.2.2 X-Ray Diffraction

High angle x-ray diffraction was carried out using a four-circle 29cm base goniometer. The $\theta - 2\theta$ scans were performed with \mathbf{q} along the surface normal (out-of-plane geometry) or with a component in the film plane (in-plane geometry). The out-of-plane scans are used to probe the film's crystallinity along the growth direction, while in-plane scans give information about the structure in the film plane. ϕ scans are performed by positioning the detector at a Bragg peak and rotating the film around the growth direction. The appearance of sharp ϕ peaks matching the crystal's symmetry means the film is epitaxial in nature [41, 42].

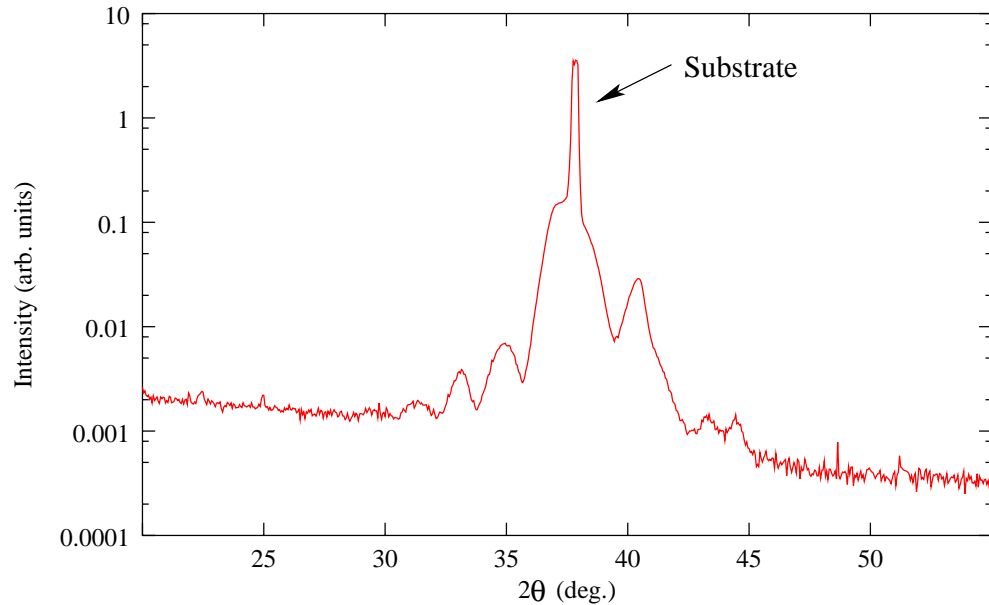


Figure 3.8: High angle $\theta - 2\theta$ aligned with the buffer.

Figure 3.8 shows a $\theta - 2\theta$ scan with $\mathbf{q} \parallel [11\bar{2}0]$ of the substrate. Labeled in the plot are the Al_2O_3 substrate $(11\bar{2}0)$, Re buffer $(10\bar{1}0)$, and $(11\bar{2}0)$ superlattice peaks. The fringes on the plot, resulting from the constructive interference between x-rays scattering from the bottom and top surfaces of the Re buffer layer, are further evidence that the buffer layer is very smooth, the interface roughness from the x-ray reflectivity

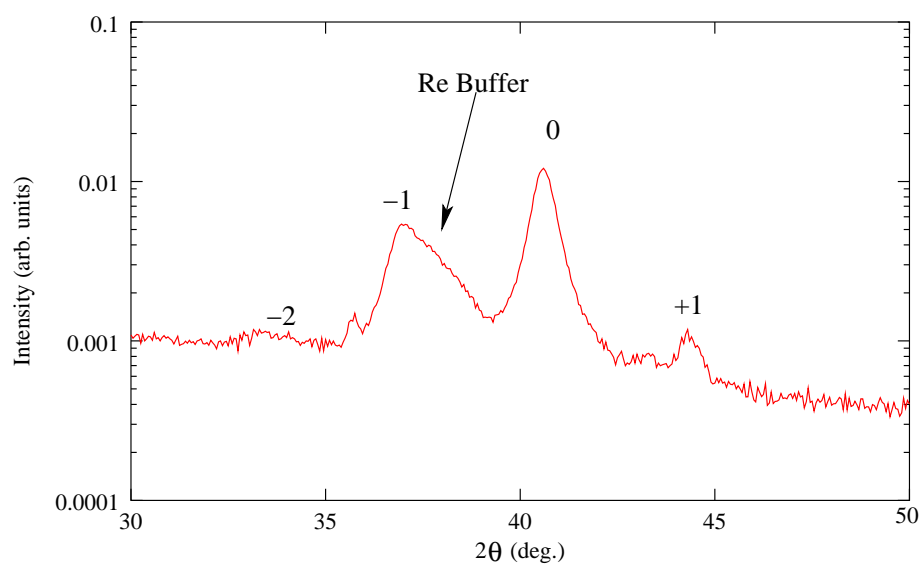


Figure 3.9: High angle $\theta - 2\theta$ aligned with the superlattice.

fit being $\sim 1 \text{ \AA}$. To see the superlattice peaks more clearly (shown in figure 3.9), the $\theta - 2\theta$ scan is performed with the sample's θ misaligned by 1° with respect to 2θ . The substrate rocking curve is $\sim 0.08^\circ$ wide, while that of the superlattice is much wider ($3^\circ - 5^\circ$) than the substrate rocking curve, so at a misalignment of 1° the detector is still sensitive to the superlattice structure. Further examination of the rocking curves show that the superlattice does not coincide with the substrate peak. The samples grow slightly tilted ($\sim 0.5^\circ$) with respect to the substrate. In-plane scans in figures 3.10 and 3.11 show that samples are epitaxial with the hcp [0001] axis, the c-axis, in the sample plane. Figure 3.10 shows a $\theta - 2\theta$ scan with \mathbf{q} along the Re buffer $(11\bar{2}0)$ reflection. The substrate $(03\bar{3}0)$, Re buffer $(11\bar{2}0)$ and superlattice $(11\bar{2}0)$ reflections are labeled. Aligning \mathbf{q} along the superlattice $(11\bar{2}0)$ and rotating about the growth direction produces the ϕ scan plotted in figure 3.11. The two peaks 180° apart, matching the crystal's in-plane symmetry, come from the $(11\bar{2}0)$ and $(2\bar{1}10)$ planes. The same symmetry and peak position is also seen for the Re buffer layer, proving that the sample is indeed epitaxial.

Strain in the Co layer is also a concern since it can affect the magnetization in the samples. If the strain were the same for all samples, then the main superlattice peak position would be the weighted average of the Re and Co lattice parameters:

$$d_{\text{SL}} = (t_{\text{Co}}d_{\text{Co}} + t_{\text{Re}}d_{\text{Re}})/(t_{\text{Co}} + t_{\text{Re}}), \quad (3.5)$$

where d_{SL} is the lattice parameter determined from Bragg's law using the position of the main superlattice peak [43]. Equation 3.5 can be rewritten as equation as

$$\frac{d_{\text{SL}}(t_{\text{Co}} + t_{\text{Re}})}{t_{\text{Co}}} = d_{\text{Co}} + d_{\text{Re}} \frac{t_{\text{Re}}}{t_{\text{Co}}}. \quad (3.6)$$

Hence, plotting $d_{\text{SL}}(t_{\text{Co}} + t_{\text{Re}})/t_{\text{Co}}$ versus $t_{\text{Re}}/t_{\text{Co}}$, using the values of t_{Co} and t_{Re} from the low angle x-ray fits, should yield a straight line if d_{Co} and d_{Re} are the same for all samples. Figure 3.12 is such a plot, where the solid line is a linear fit to the

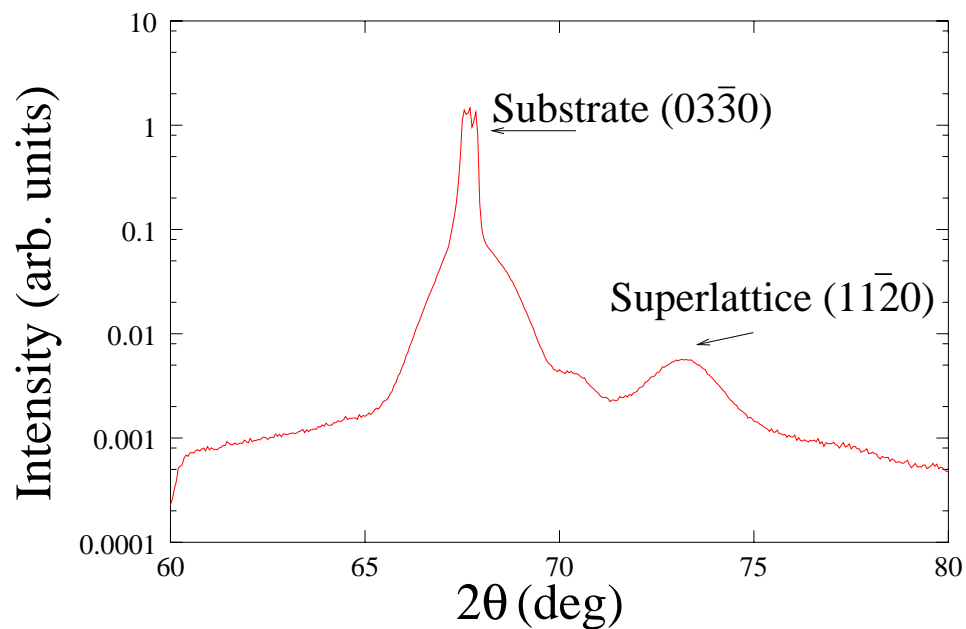


Figure 3.10: High angle in-plane $\theta - 2\theta$ scan with \mathbf{q} along the $[11\bar{2}0]$ direction of the buffer layer and the superlattice. The substrate $(03\bar{3}0)$, buffer layer, and superlattice $(11\bar{2}0)$ peaks are labeled.

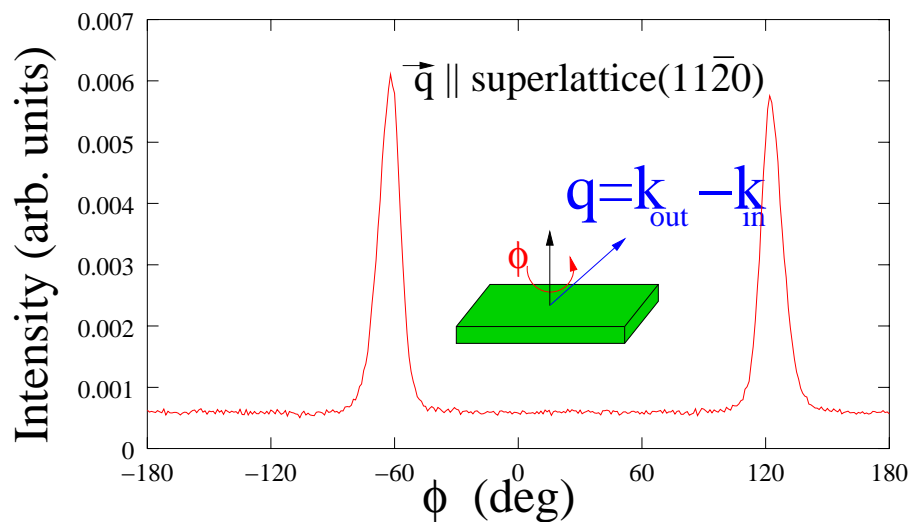


Figure 3.11: High angle ϕ scan obtained by rotating the sample about the growth direction with \mathbf{q} fixed along the superlattice $(11\bar{2}0)$.

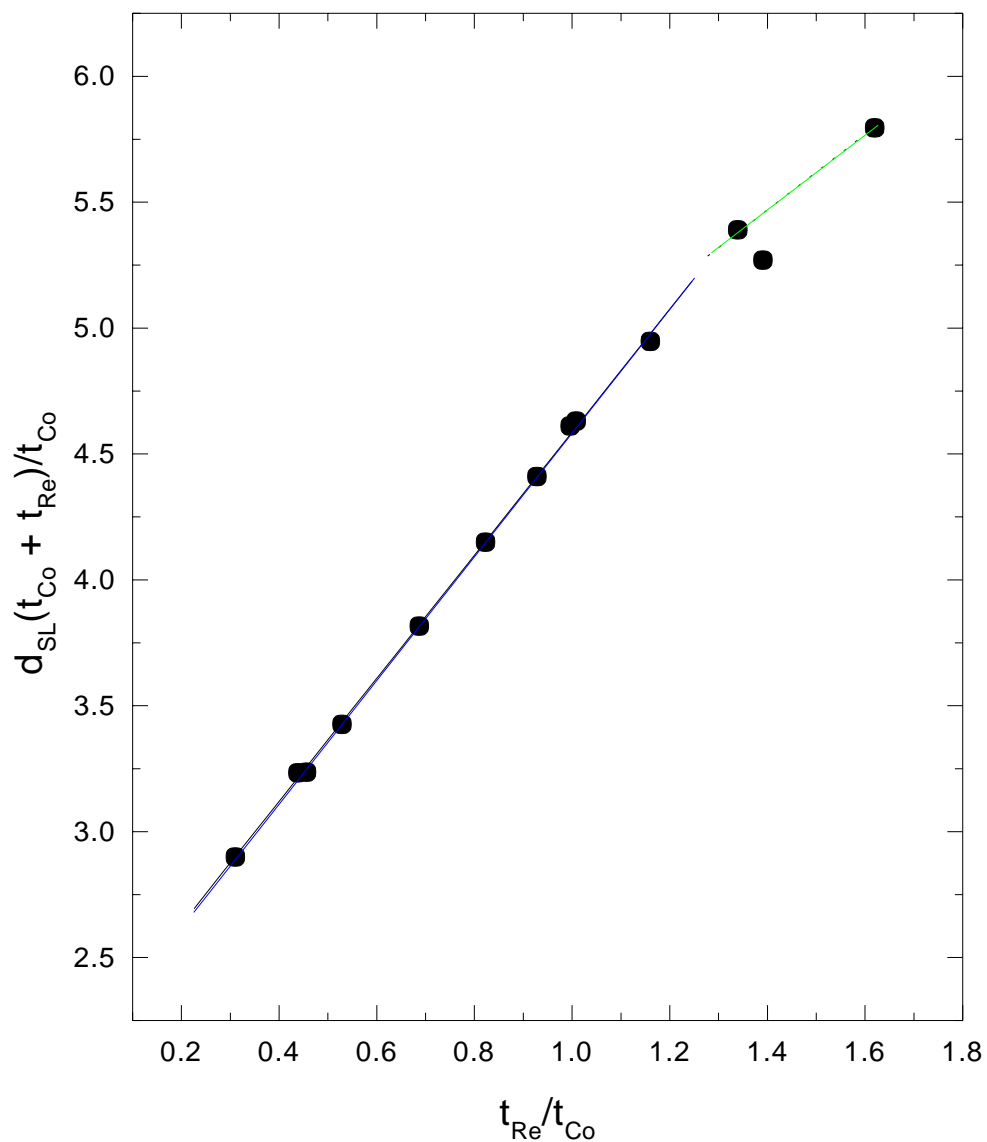


Figure 3.12: $d_{SL}(t_{Co} + t_{Re})/t_{Co}$ plotted as a function of t_{Re}/t_{Co} , using the values of t_{Co} and t_{Re} obtained from low angle x-ray reflectivity fits. The blue line is a fit to the data for $t_{Re}/t_{Co} < 1.2$, yielded $d_{Co} = 2.13 \text{ \AA}$ and $d_{Re} = 2.46 \text{ \AA}$. The green line is a guide to the eye.

data for $t_{\text{Re}}/t_{\text{Co}} \leq 1.2$ with $d_{\text{Co}} = 2.13 \text{ \AA}$ and $d_{\text{Re}} = 2.46 \text{ \AA}$. This is approximately a 2.5% increase with respect to the bulk Re ($10\bar{1}0$) interplanar spacing (2.39 \AA), and a decrease in the Co bulk plane spacing (2.17 \AA). This makes sense considering the in-plane lattice spacings. For bulk Co ($1\bar{2}10$), the interplanar spacing is 1.25 \AA , and the in-plane spacing for bulk Re is 1.38 \AA . Hence, to accommodate the strain, the in-plane lattice parameter of Re must decrease and Co's in-plane lattice constant must increase, causing the out-of-plane d_{Co} to decrease and the out of plane d_{Re} to increase. For the samples with $t_{\text{Re}}/t_{\text{Co}} > 1.2$ the main superlattice peak was difficult to identify due to its proximity to the buffer layer peak, but it seems that the linear relationship is no longer obeyed, presumably due to an increase in strain-related defects.

3.2.3 Summary

In previous studies of Co/Re superlattices, samples were grown on glass and oriented with the $[001]$ direction parallel to the surface normal, with no indication of in-plane epitaxy [44, 45, 32]. Our superlattices were grown on Al_2O_3 $[11\bar{2}0]$ substrates. The x-ray diffraction scans show that the samples grow epitaxially with the $[10\bar{1}0]$ direction parallel to the growth direction and the $[0001]$ direction of the sample parallel to the $[0001]$ direction of the substrate. From the low angle modeling we find that the samples are smooth with Co-Re interface roughness of $\sim 5 \text{ \AA}$. This is similar to the reported value of 4.1 \AA for c-axis oriented Co/Re superlattices grown on glass [44].

3.3 Magnetic Measurements

3.3.1 Magneto-Optic Kerr Effect

The Magneto-Optic Kerr Effect (MOKE) hysteresis loops were measured on a custom built instrument shown in the diagram of figure 3.13. The MOKE experiment measures the rotation of the polarization of linearly polarized light upon reflecting from

a magnetic material. The rotation of the polarization occurs because of the off diagonal terms, magneto-optic (Voigt) constants, in the dielectric tensor [46].

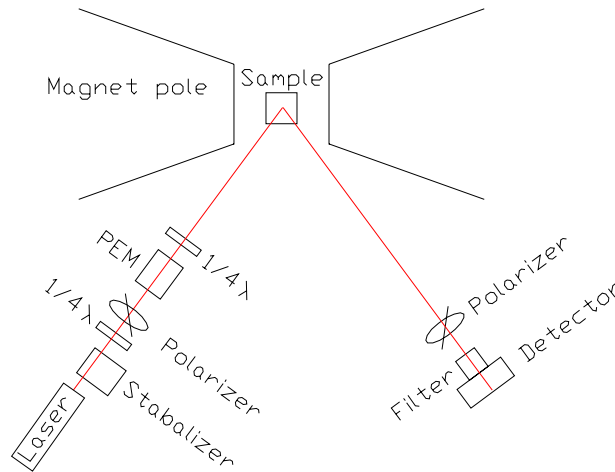


Figure 3.13: A block diagram of the MOKE setup.

We use an AC - lockin technique, where the incident laser light's polarization is modulated by a photoelastic modulator (PEM) prior to reflecting from the sample. Light is provided by a 4 mW polarized He-Ne laser. Since changes in the laser intensity show up as noise and drift in the MOKE signal, an intensity stabilizer is necessary. Light from the stabilizer is linearly polarized in the same direction as the laser. To allow the incident polarization to be rotated without changing the laser, a $1/4 - \lambda$ -plate is placed before the primary polarizer. Next the linearly polarized light is modulated by the PEM. Because the PEM is slightly birefringent, a $1/4 - \lambda$ -plate is used to cancel this effect. The sample rotates the polarization due to the Kerr effect upon reflecting and the reflected light passes through an analyzer set at extinction. This only allows the rotated component of polarized light through to the detector. To minimize the effect of other lights in the room, a laser notch filter was placed on the detector.

3.3.2 Vibrating Sample Magnetometry

The principle behind vibrating sample magnetometry (VSM) is a relatively simple application of Faraday's law of magnetic induction. If a magnet (in this case a magnetic sample) is moved through a coil of wire, the change in flux through the coil induces a voltage in it. In the VSM the sample vibrates at a fixed frequency (73 Hz) near a set of pickup coils which induces a voltage signal measured by a lockin amplifier. To convert the measured voltage into emu a standard nickel sample is measured at saturation. This calibration factor is then applied to the sample of interest.

Like the MOKE experiment, the VSM is designed so that the sample may be rotated through a full 360° . The VSM also has a closed cycle cryostat allowing temperature dependent measurements from 20 K to 300 K . Unfortunately the cryostat's vibrations adds noise in the signal, so a relay to turn off the cold head during measurements was recently installed to prevent this.

3.3.3 SQUID Magnetometry

All SQUID measurements were performed on a commercial Quantum Design instrument. SQUID stands for Superconducting Quantum interference Device, and is simply the most sensitive magnetic flux detector known. At the heart of any SQUID is a superconducting loop with a Josephson junction. Any flux change through the loop will lead to a change in phase difference across the junction which gives rise to a measurable voltage difference. If the current in the squid loop is kept constant then the magnitude of the voltage signal is directly proportional to the change in flux through the loop [47].

In our SQUID the pickup coils are arranged in a balanced second-derivative configuration designed to eliminate unwanted signals from the superconducting magnet or any other source of magnetic field. This arrangement is called a gradiometer and

measures d^2B/dz^2 .

3.3.4 Ferromagnetic Resonance

Ferromagnetic resonance (FMR) measurements were made at Miami University at Ohio by M. J. Pechan and Z. Hilt. The external magnetic field was applied in the sample plane. The sample was mounted film side down in a 35 GHz cavity. Angular dependent data were taken by rotating the magnet about the cavity. The effective magnetization and the anisotropy constants were determined by fitting the resonance line position to the resonance equation for a flat disk [48]. The resonance equation is

$$\left(\frac{\omega_o}{\gamma}\right)^2 = [H \cos(\phi - \phi_H) + 4\pi M_{eff} + (H_{A1} - 2H_{A2}) \cos^2 \phi - 2H_{A2} \cos^4 \phi] \\ \times [H \cos(\phi - \phi_H) + (H_{A1} + H_{A2}) \cos(2\phi) - H_{A2} \cos(4\phi)],$$

where ω_o is the source frequency (35 GHz), $\gamma = g\mu_B/\hbar$ is the gyromagnetic ratio, g is the g factor for Co ($g_{Co} = 2.19$), M_{eff} is the effective magnetization, ϕ and ϕ_H are the angles the magnetization and the applied field make with the c -axis of the substrate. At 35 GHz, ϕ and ϕ_H are approximately the same. H_{A1} and H_{A2} are the first and second order anisotropy fields given by $H_{Ai} = 2K_i/M_{sat}$. K_1 and K_2 are the anisotropy constants of a uniaxial anisotropy of the form $U_k = K_1 \sin^2 \phi + K_2 \sin^4 \phi$ and M_{sat} is the saturation magnetization measured by the SQUID.

Figure 3.14 shows the resonance line position as a function of angle for a Co/Re superlattice. The points are the data and the line is a fit using equation 3.7. From the fit, the K_1 and K_2 values are plotted in figure 4.2 and M_{eff} is plotted in figure 3.15, along with M_{sat} from the SQUID. The error bars are due to the uncertainty in the cobalt thickness and the total sample area. These samples were Co/Re superlattices with fixed t_{Co} and different t_{Re} . These measurements are discussed further in section 4.1.

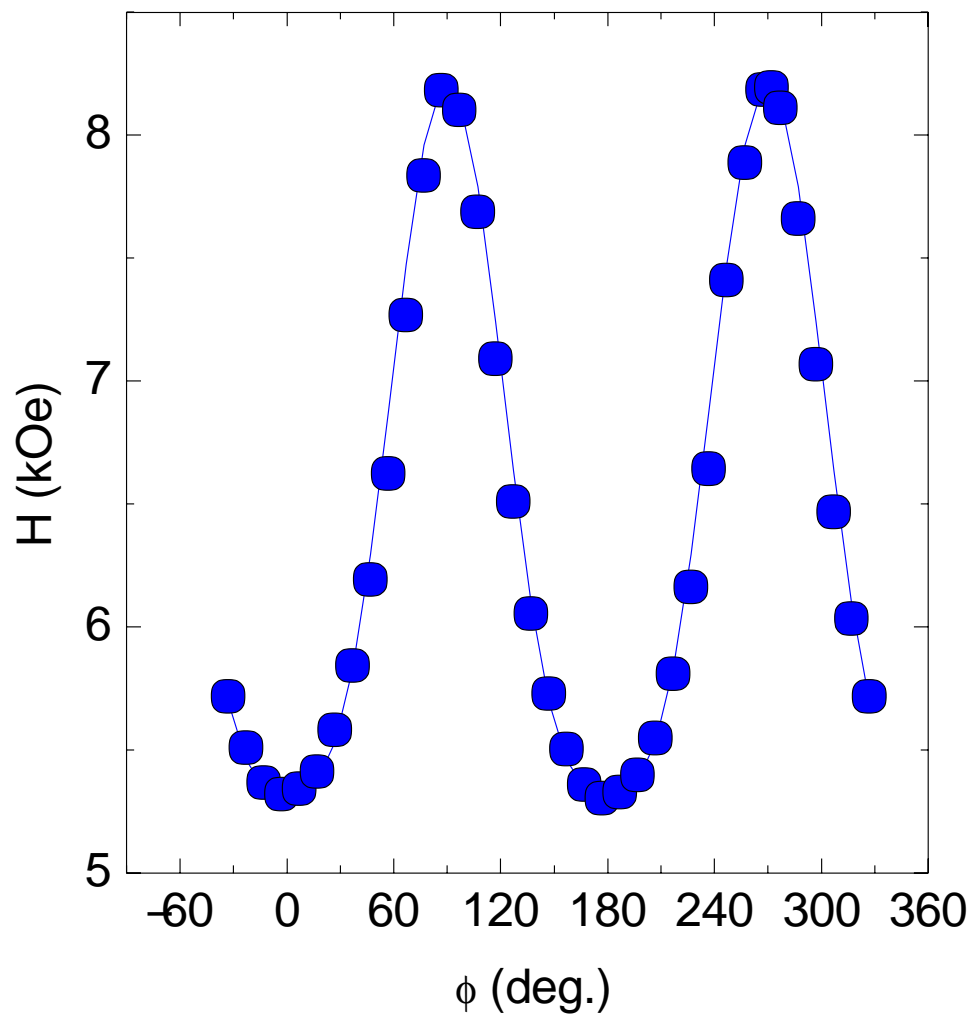


Figure 3.14: Resonant line position as a function angle for a superlattice with $t_{Co} = 20 \text{ \AA}$
 $t_{Re} = 6 \text{ \AA}$.

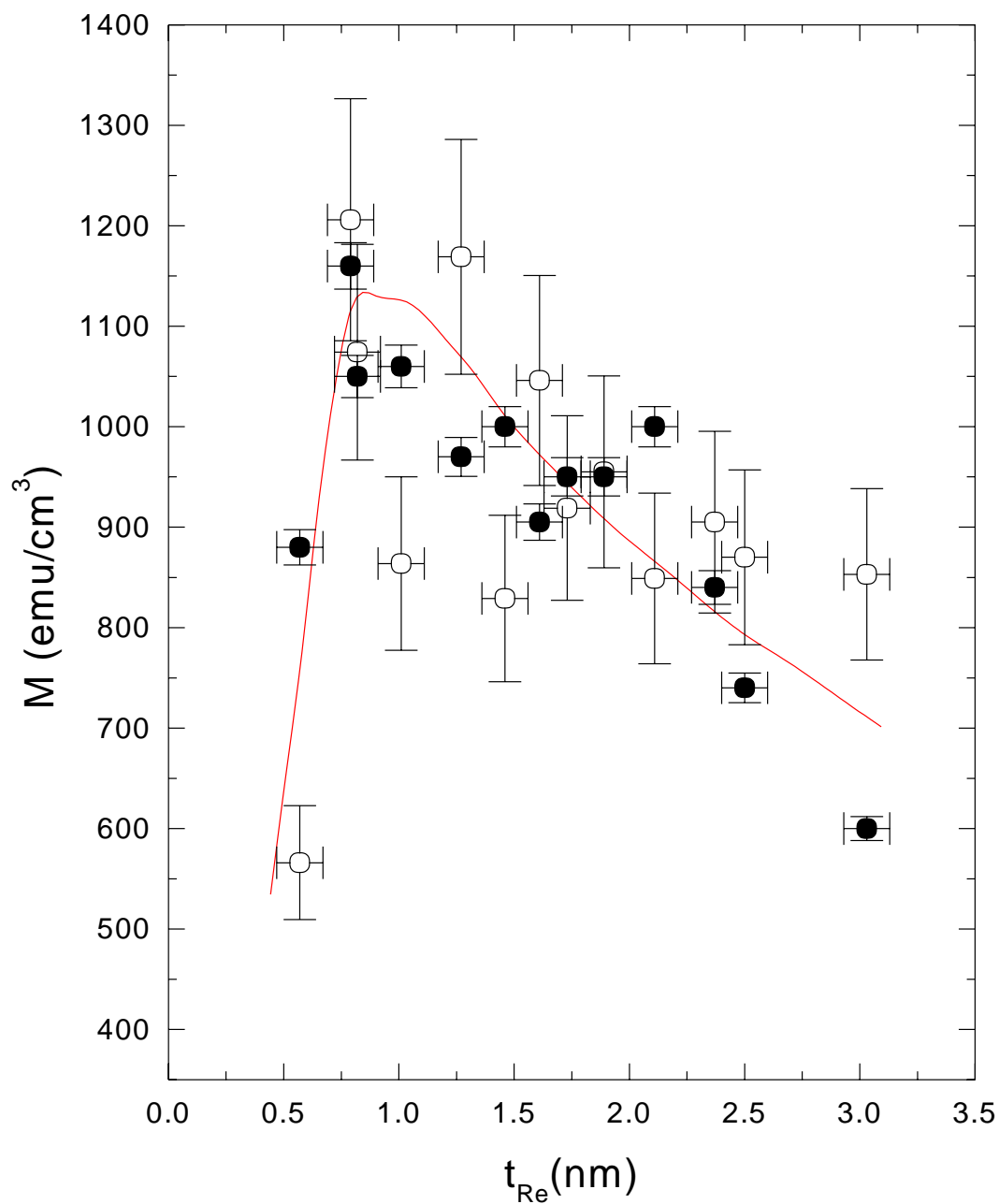


Figure 3.15: Saturation magnetization measured by SQUID(●) magnetometry and the effective magnetization (○) from the FMR experiment. All samples have $t_{Co} \sim 20\text{\AA}$. The line is a guide to the eye.

3.4 Neutron Reflectivity

Neutron reflectivity is an invaluable tool for investigating the magnetic response of a thin film. By choosing the q range of the incident neutrons, different magnetic alignments can be studied. For example, by setting q near $1/\Lambda$ ($1/\text{superlattice period}$) the ferromagnetic moment is probed, or with q near $1/2\Lambda$, the antiferromagnetic moment in an antiferromagnetic superlattice system is probed. With polarization analysis, the vector magnetic moment can be measured. This is better than standard methods of measuring the magnetic response such as SQUID, VSM, or MOKE, since they only probe the component of M along the applied magnetic field.

The neutron reflectivity experiments were carried out at the Intense Pulsed Neutron Source (IPNS) at Argonne National Laboratory on the POSY instrument. At IPNS neutrons are created by spallation. All spallation sources have three major components: a linear proton accelerator (LINAC), a rapid cycling synchrotron (RCS), and a target. Protons are accelerated in the LINAC and injected into the RCS at 50MeV where the protons are further accelerated to 450MeV before they hit the enriched uranium target 30 times every second. Once neutrons are created, they are allowed to thermalize in a solid methane moderator before they travel down the beam pipes to the experiment.

For completeness the main features of the instrument are summarized below. POSY, like all instruments at a pulsed source, is a time of flight spectrometer, shown in figure 3.16. (A detailed description of POSY can be found in reference [49].) Once a pulse of neutrons reaches the instrument, they are polarized with their spins parallel to applied field at the sample by an Fe/Cr supermirror with an efficiency of nearly 100% for neutrons with $4\text{\AA} < \lambda$ and 95% for neutrons with λ up to 8\AA . Next the neutrons pass through a set of spin-flippers, which flips the spin of every other pulse so that the spin-up and spin-down reflectivities can be measured nearly simultaneously. Then the neutrons scatter from the sample on to an analyzing mirror which lets spin-up neutrons

pass through while reflecting the spin down neutrons. This separates the spin-up and spin-down neutrons spatially in the linear detector allowing their intensity to easily be compared. A typical neutron scan is shown in figure 3.17.

To obtain the maximum possible information from the neutron experiment we measured all four possible neutron cross sections R_{++} , R_{--} , R_{+-} and R_{-+} over a q range up to and including the Bragg reflection of the antiferromagnetic peak. The first subscript denotes the polarization direction of incident neutrons and the second subscript denotes the polarization direction of the neutrons reflected from the sample.

The integrated AF peak intensity is proportional to the square of the sublattice magnetization, M_{AF}^2 . M_{AF}^2 has components $M_{AF\parallel}$ parallel to H and $M_{AF\perp}$ perpendicular to H . These two components can be separated by analyzing the spin of the scattered neutron. A neutron will only flip its spin if it scatters from another particle with a spin perpendicular to its own spin. So, $M_{AF\parallel}$ is associated with the R_{++} and R_{--} reflections and $M_{AF\perp}$ with R_{+-} and R_{-+} . From these two components we can plot the angle the AF moment makes with H , as shown in figure 4.7.

3.5 Magnetotransport

Normally, resistivity measurements are made using a four point van der Pauw technique [50]. The contacts are arranged either in a straight line or at the center of each edge of a square sample (see figure 3.18). Samples were cut to nearly 3 mm \times 3 mm to fit in the 5.5 T superconducting magnet and liquid helium cryostat used for SQUID magnetometry. A constant current is applied between the outer two contacts and a voltage is measured between the center contacts in the linear geometry. To confirm that the contacts are ohmic, $I - V$ curves were measured. They were found to be linear over a range of $\pm 2I$ where I is the sensing current used to measure the resistance.

The van der Pauw technique [50] works well for isotropic materials like polycrystalline or amorphous thin films, but not for our anisotropic superlattices. In this case,

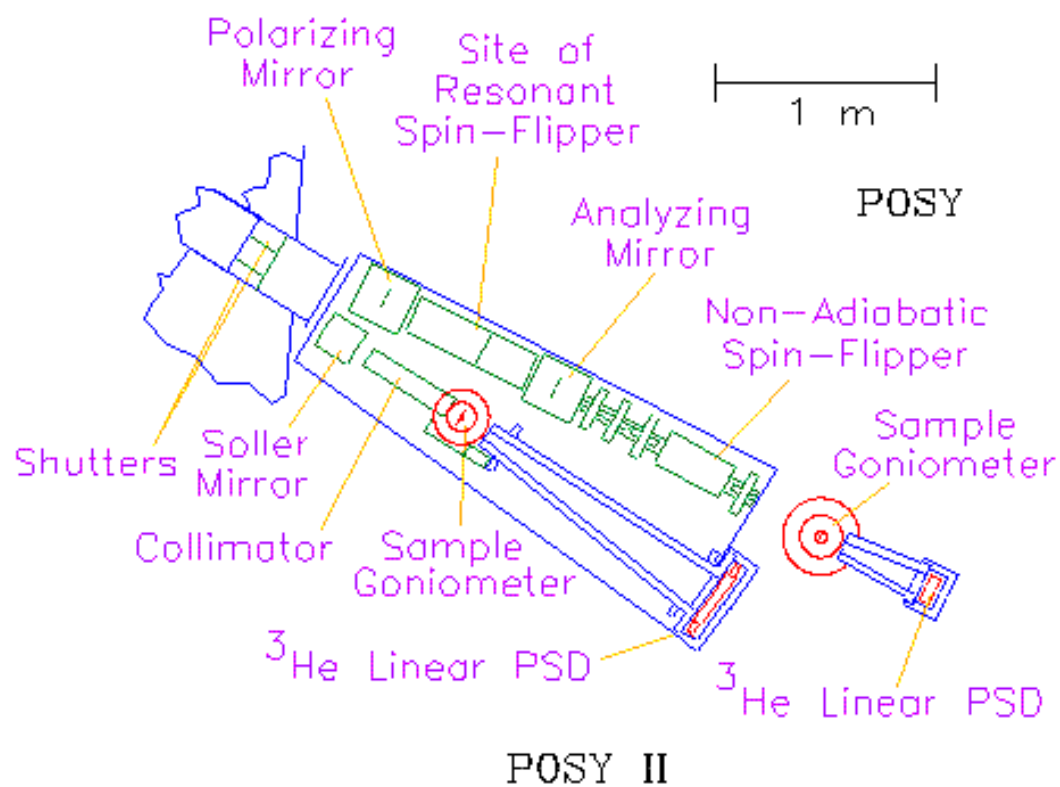


Figure 3.16: The POSY and POSY II instruments. POSY is shown the upper beam path, while POSY II is the lower beam path. All measurements were performed on POSY.

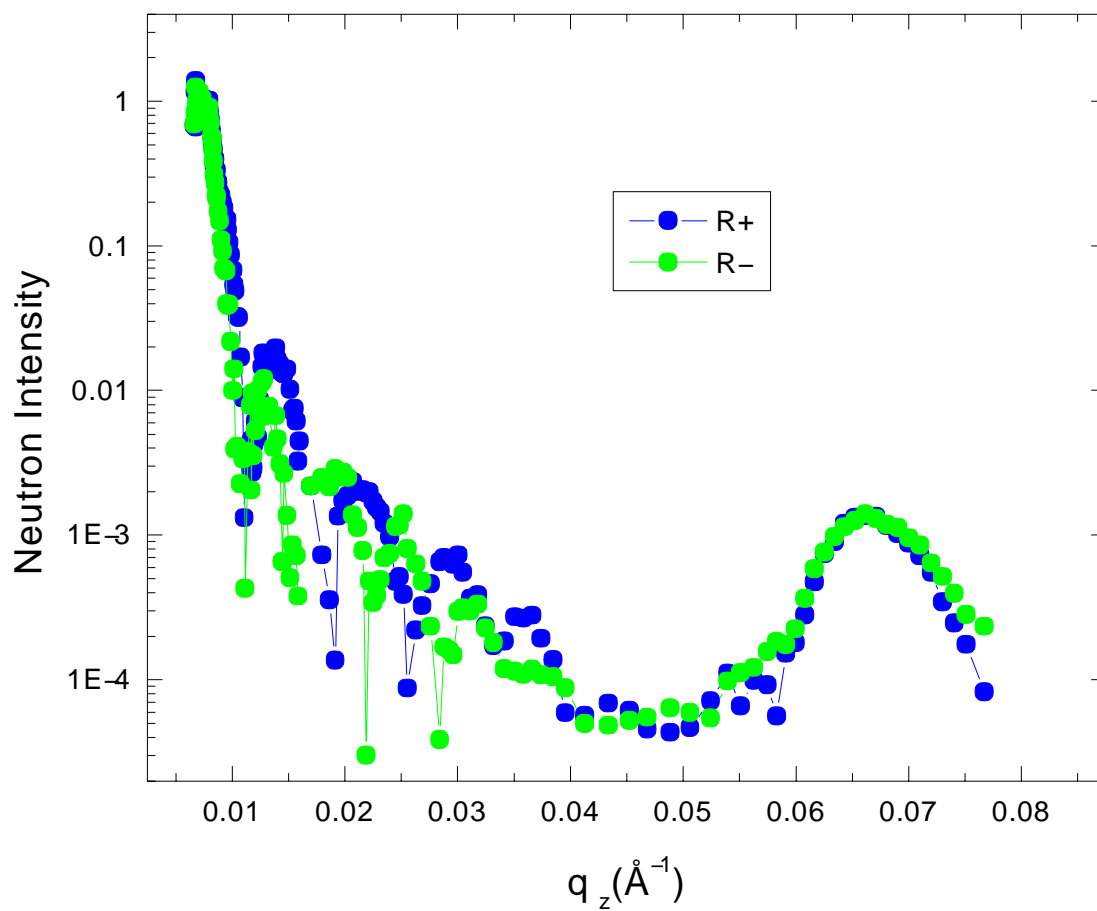


Figure 3.17: Typical neutron reflectivity scan over a q range up to the antiferromagnetic peak (at $q_z \sim 0.065$).

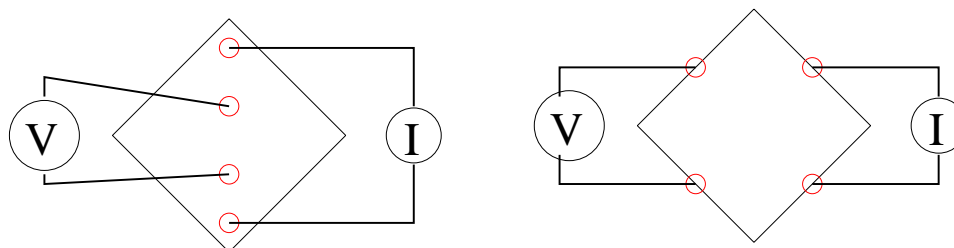
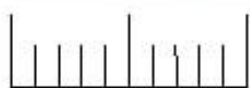
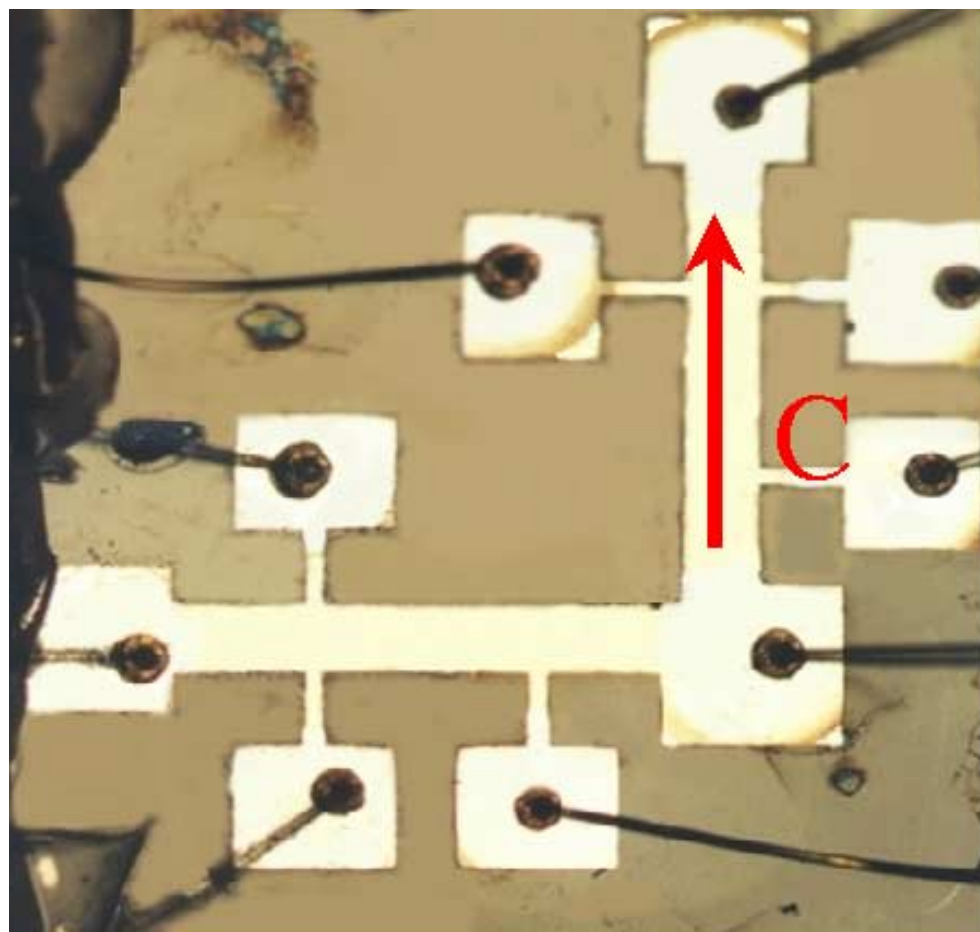


Figure 3.18: Contact geometries

small deviations in contact placement in relation to the anisotropy axis give different results. To prevent this problem, the samples were patterned by photolithography into the shape shown in figure 3.19. By aligning one arm of the pattern along the anisotropy axis, the c -axis, the resistance can be measured in the four following geometries 1) $H \parallel c, H \parallel I$, 2) $H \parallel c, H \perp I$, 3) $H \perp c, H \parallel I$, 4) $H \perp c, H \perp I$. Also, the resistance measurements with $I \parallel c$ and $I \perp c$ can be made on the same sample piece with exactly the same contact spacing.



0.5 mm

Figure 3.19: Photograph of a sample patterned with photolithography. The direction of the c -axis is marked by the arrow. The gold wire bonds can be seen.

Chapter 4

Results

4.1 In-plane Magnetic Anisotropy

Figure 4.1 shows the magnetic hysteresis loops measured by VSM for two different samples, one with $t_{Re} = 7 \text{ \AA}$ and the other with $t_{Re} = 14.6 \text{ \AA}$, and both with $t_{Co} = 18.9 \text{ \AA}$. The magnetic field was applied parallel and perpendicular to the c -axis of the substrate. In the $t_{Re} = 14.6 \text{ \AA}$ film, the loop is square for $H \parallel c$ and completely sheered for $H \perp c$. This confirms that the in-plane structural anisotropy, due to the in-plane epitaxy, causes the in-plane magnetic anisotropy. For the $t_{Re} = 7.9 \text{ \AA}$ film both the $H \parallel c$ and $H \perp c$ loops are sheered, which indicates that adjacent Co layers are coupled antiferromagnetically. The change in the slope in the $H \parallel c$ loop at $H \sim 1130 \text{ Oe}$ is a signature of a spin-flop transition, similar to the spin-flop transition seen in traditional antiferromagnets. A detailed discussion of the spin-flop transition is given in sections 3.4 and 4.3. Figure 3.15 shows the saturation magnetization measured by the SQUID and the M_{eff} extracted from the FMR fits. Notice that for $t_{Re} > 10 \text{ \AA}$ the values of M_{sat} and M_{eff} agree within the experimental uncertainty. This means that there is very little surface or interface anisotropy perpendicular to the sample plane. Also, for $t_{Re} > 10 \text{ \AA}$ M_{sat} and M_{eff} decrease monotonically with increasing t_{Re} . If the trend is extrapolated to $t_{Re} = 0$, one obtains $M(t_{Re} = 0) \sim 1400 \text{ emu/cm}^3$, which matches the bulk value of Co. Strain is an unlikely cause of this decrease since the strain was shown to be the same for all samples in section 3.2.2. Instead, the Re at the interface probably mag-

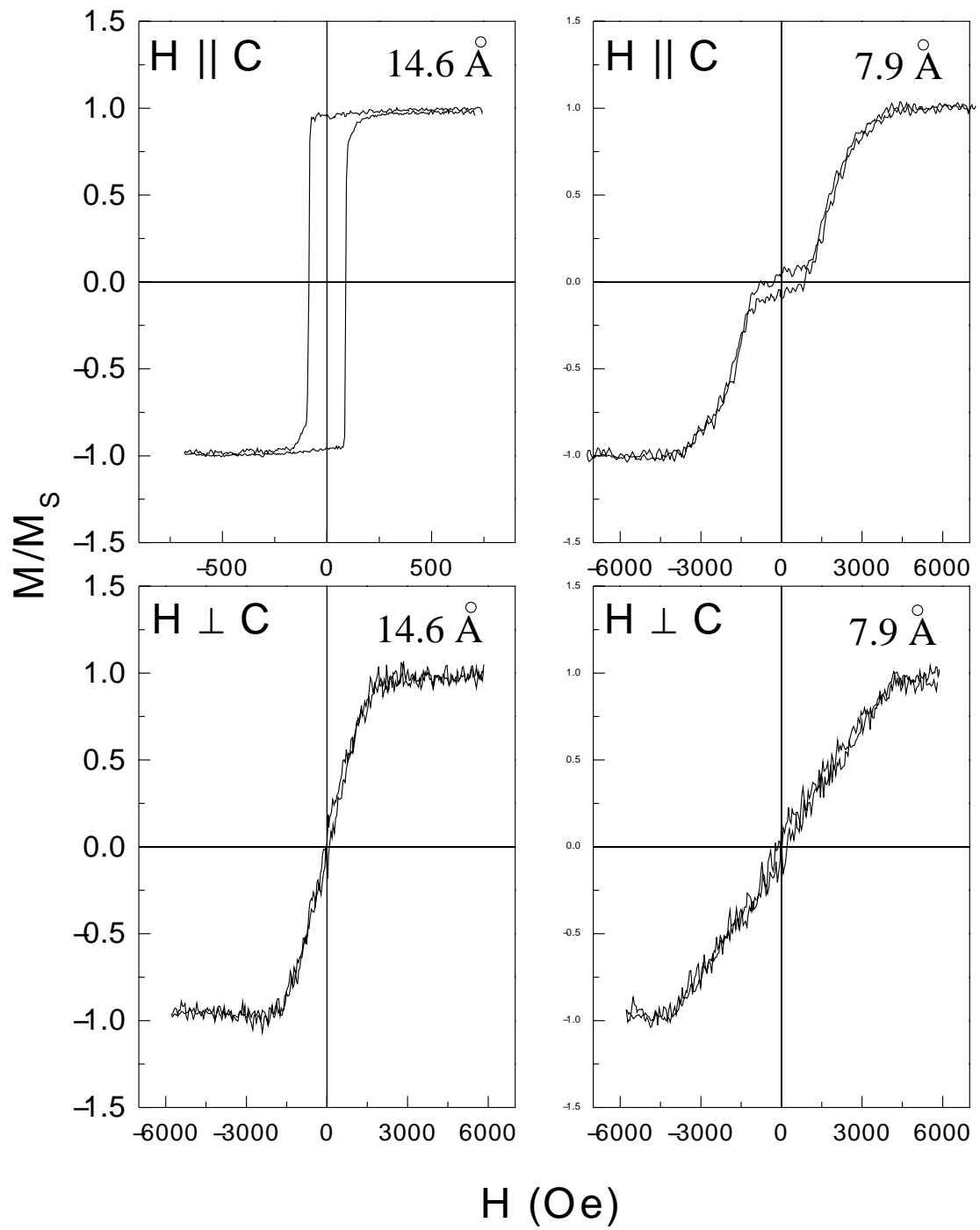


Figure 4.1: Hysteresis loops measured at room temperature for two different samples with $t_{Co} \sim 20 \text{ \AA}$ and $t_{Re} = 14.6 \text{ \AA}$ and $t_{Re} = 7.9 \text{ \AA}$ with H applied parallel and perpendicular to the c -axis.

netically disorders the nearby Co. The anisotropy constants K_1 and K_2 as function of t_{Re} are shown on figure 4.2. K_1 starts out small for small t_{Re} , but increases and eventually saturates at $\sim 0.7 \times 10^6 \text{erg/cm}^3$. K_2 behaves similarly, saturating at $0.2 \times 10^6 \text{erg/cm}^3$. The thinnest t_{Re} actually shows a negative K_2 . This could be caused by the interface roughness, which could alter the magnetic properties of the Co near the interface. The measured K_1 and K_2 are lower than the values listed for bulk Co [2], $4.1 \times 10^6 \text{erg/cm}^3$ and $1.0 \times 10^6 \text{erg/cm}^3$. Studies of $\text{Co}(10\bar{1}0)/\text{Cr}(211)$ superlattices [51] show a similar behavior for the anisotropy constants, with $K_1 = 1.8 \times 10^6 \text{erg/cm}^3$ and $K_2 = 0.55 \times 10^6 \text{erg/cm}^3$. The ratio of $K_1/K_2 \sim 3.5$ is similar to the b-axis oriented single layer Co films approximately 500\AA thick. But in the single layer Co films $K_1 = 3.4 \times 10^6 \text{erg/cm}^3$ and $K_2 = 1.0 \times 10^6 \text{erg/cm}^3$ [52] which are about 5 times larger than in the Co/Re superlattices. This could be due to the strain in the Co layer described earlier in section 3.2.2.

The magnetic hysteresis loops observed by the MOKE experiment with $H \parallel c$ are shown in figure 4.3. Samples with $t_{Re} < 8.2 \text{\AA}$, and $18.9 \text{\AA} < t_{Re} < 21.1 \text{\AA}$ are sheered or have steps, indicating the presence of antiferromagnetic coupling. Similar features have been observed in $\text{Fe}/\text{Cr}(211)$ superlattices [37]. All other values t_{Re} have square loops, indicating ferromagnetic coupling. This is possible evidence for oscillatory exchange coupling as a function of t_{Re} , as seen in other systems such as Co/Ru , Co/Cr and Fe/Cr [53].

4.2 Surface Induced Magnetic Perpendicular Anisotropy

Figure 4.4 (a) shows hysteresis loops for a sample with $t_{Re} = 12.4 \text{\AA}$ and $t_{Co} = 21.1 \text{\AA}$ measured with $H \parallel c$, $H 45^\circ c$, and $H \perp c$. For this Re thickness the layers are either ferromagnetically coupled or uncoupled. With $H \parallel c$ the loop is square, while for $H \perp c$ the loop is sheered, confirming the expected uniaxial anisotropy along the c-axis. The angular dependence of the remanent magnetization (M_r) and the coercive field

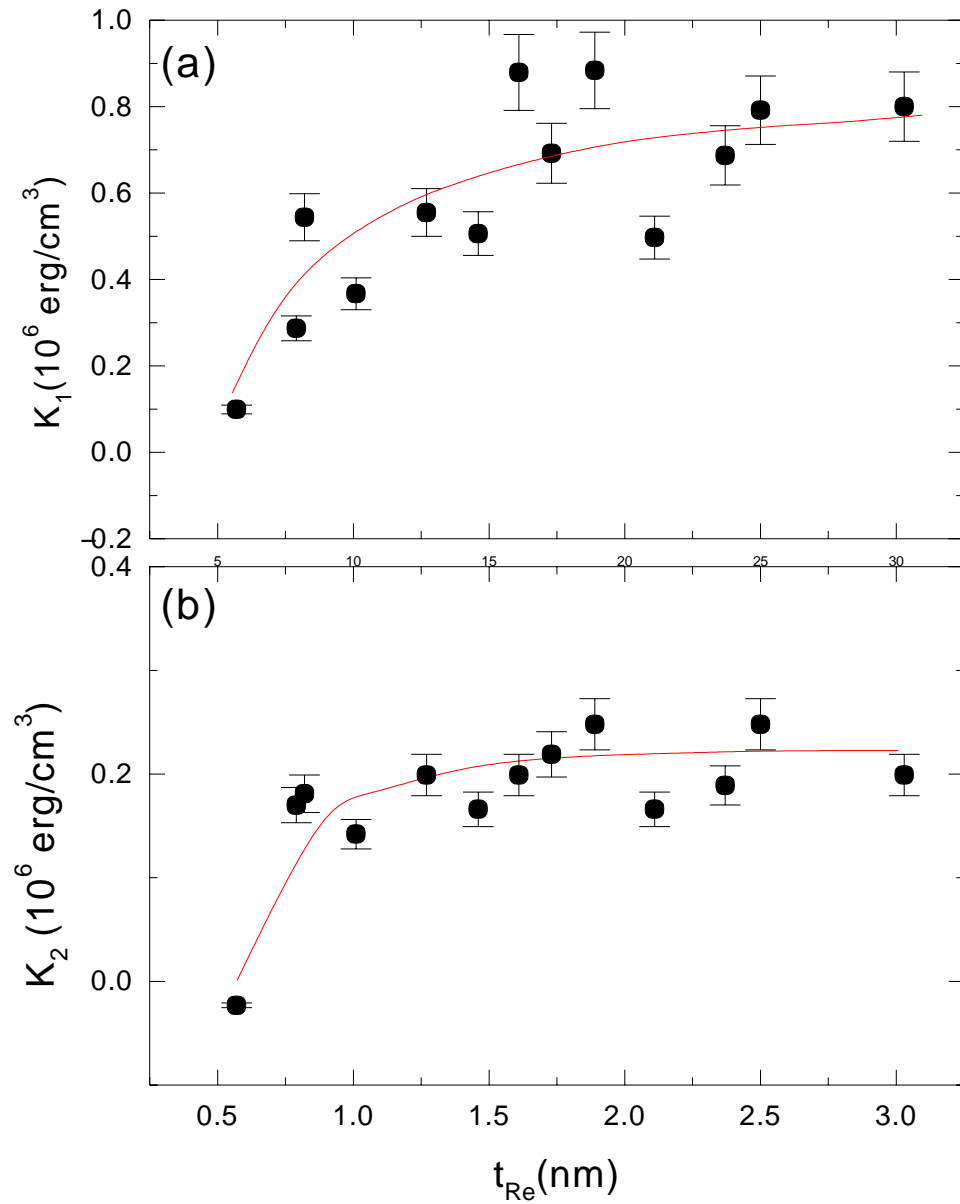


Figure 4.2: The anisotropy constants K_1 (a) and K_2 (b) as a function of Re thickness. All samples have a $t_{Co} \sim 20 \text{ \AA}$. The lines are guides to the eye.

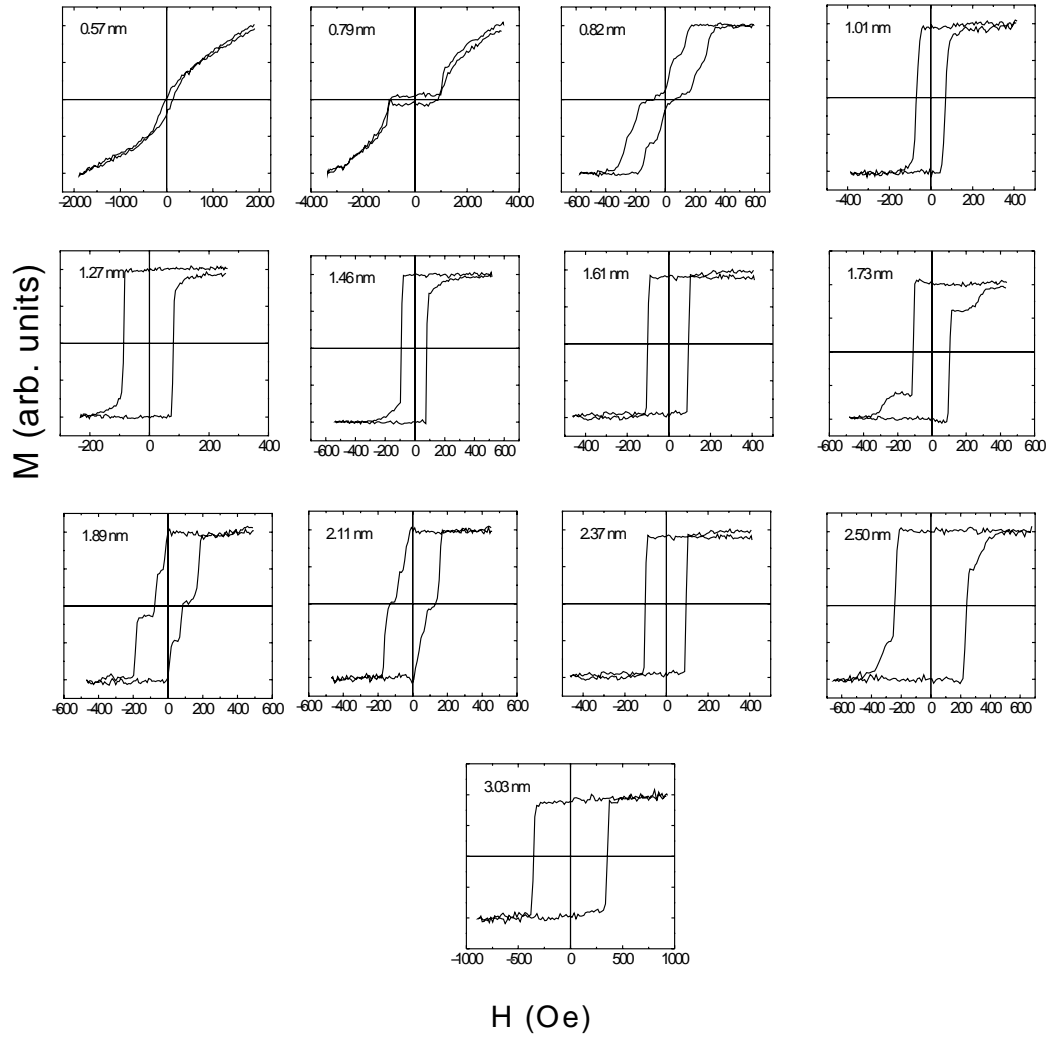


Figure 4.3: MOKE hysteresis loops measured with $H \parallel c$. Each loop is labeled by the Re layer thickness. All samples have a $t_{Co} \sim 20 \text{ \AA}$.

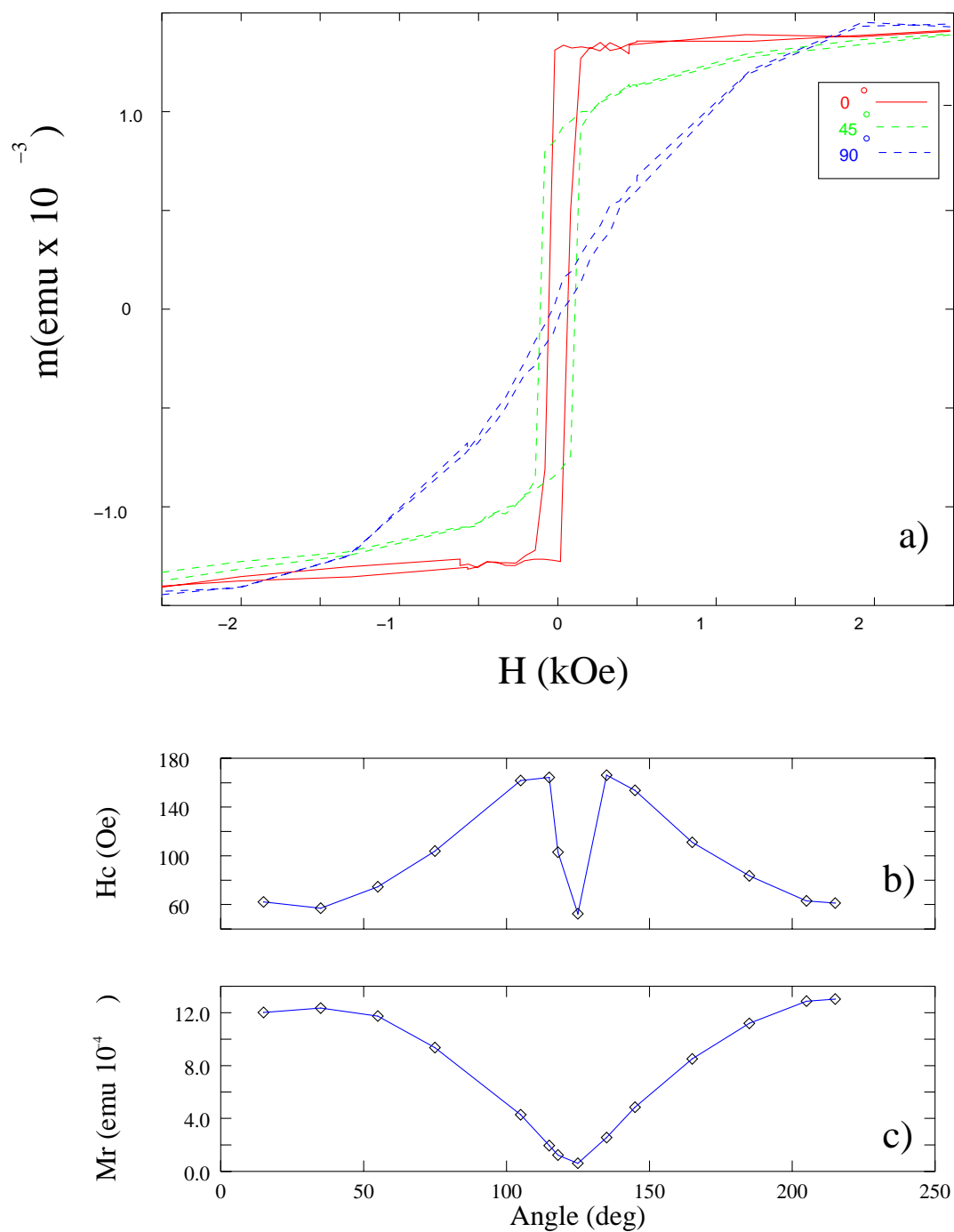


Figure 4.4: (a) Three hysteresis loops a $H \parallel c$, H 45° c , and $H \perp c$. (b) M_r and (c) H_c as function of angle between H and c for a $t_{Co} = 21 \text{ \AA}$ and $t_{Re} = 15 \text{ \AA}$ superlattice.

(H_c) are plotted in Figure 4.4 (b). Notice that M_R decreases smoothly as the direction of the applied field is rotated towards the hard direction, while the H_c increases to a maximum just before dropping sharply when H is close to the hard axis. This type of angular dependence is consistent with domain wall motion as the magnetization reversal mechanism (as opposed to domain rotation or domain reversal) [2].

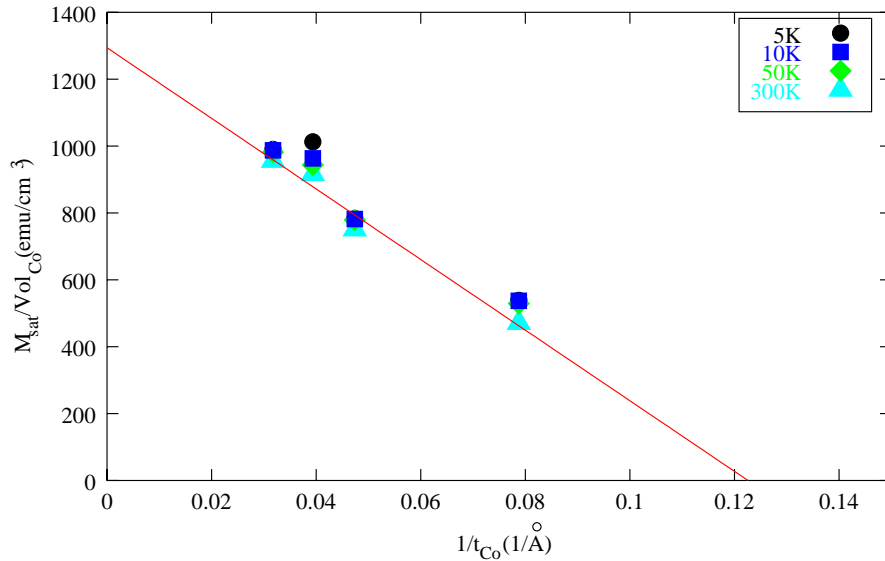


Figure 4.5: M_{sat} as a function of $1/t_{Co}$.

Figure 4.5 shows the Saturation magnetization (M_{sat}) measured by the SQUID at various temperatures between 5 K and 300 K as a function of inverse Co thickness ($1/t_{Co}$). The line is a linear fit to the 300 K data. The y-intercept of $1387 \text{ emu}/\text{cm}^3$ corresponds to the saturation magnetization for infinite t_{Co} and matches closely to $1400 \text{ emu}/\text{cm}^3$, the bulk value for Co. The x-intercept corresponds to $t_{Co} = 8.6 \text{ \AA}$, which is the thickness of Co necessary to have $M_{sat} = 0$. This implies that in each bilayer there are 8.6 \AA of magnetically dead Co. This is not surprising because at each Co-Re interface there is a roughness of $\sim 4 \text{ \AA}$, as determined from the x-ray reflectivity (see section 3.2.1).

If we plot the total out-of-plane anisotropy as a function of t_{eff} , the thickness of

magnetically active Co, a linear dependence of the form

$$K = K_{volume} + 2K_{interface}/t_{eff} \quad (4.1)$$

is expected. Plotted in figure 4.6 is the K as a function of the effective Co thickness. From a linear fit to the data we find $K_{volume} = 10.7 \times 10^6 \text{ erg/cm}^3$, which compares favorably with the expected shape anisotropy of $12.3 \times 10^6 \text{ erg/cm}^3$, and $K_{interface} = -0.074 \text{ erg/cm}^2$. The negative sign indicates that there is an out-of-plane magnetic anisotropy induced at the Co/Re interface. The interface anisotropy is much smaller than previously reported for similar systems such as thin Au/Co/Au(111) [54], where $K_{interface} = 1 \text{ erg/cm}^2$, but is nevertheless not negligible. One possible reason for the difference is that in the Au/Co/Au system Co is most likely fcc [111]-oriented, and lacks the large in-plane magnetic anisotropy. Our findings are surprising given that in our system the hcp c -axis is in the plane. To our knowledge this is the first time that such an interface-induced anisotropy has been observed.

4.3 Surface Spin Flop Transition

For our neutron reflectivity studies we chose a 20 bilayer antiferromagnetically-coupled superlattice with $t_{Co} = 17 \text{ \AA}$ and $t_{Re} = 8 \text{ \AA}$. Prior to the neutron experiment, the superlattice was characterized structurally by x-ray diffraction (figure 3.8) and reflectivity (figure 3.7), and magnetically by MOKE (figure 4.3). X-ray diffraction shows that the sample is epitaxial and oriented with $[10\bar{1}0]$ along the growth direction. The Co $[0001]$ direction lies along the c -axis of the Al_2O_3 substrate. Low angle x-ray fits yield $t_{Co} = 17 \text{ \AA}$ and $t_{Re} = 8 \text{ \AA}$ with an interface roughness of $\sim 3.4 \text{ \AA}$. The MOKE hysteresis loop with $H \perp c$ is completely sheered, passing through the origin with $H \parallel c$. Notice that $M_r = 0$, indicating that the sample is AF-coupled. The kink in the loop at $H \cong 1.1 \text{ kOe}$ is a signature of a spin-flop transition. Similar observations have been made in Fe/Cr [37, 3] and Co/Cr [55] superlattices.

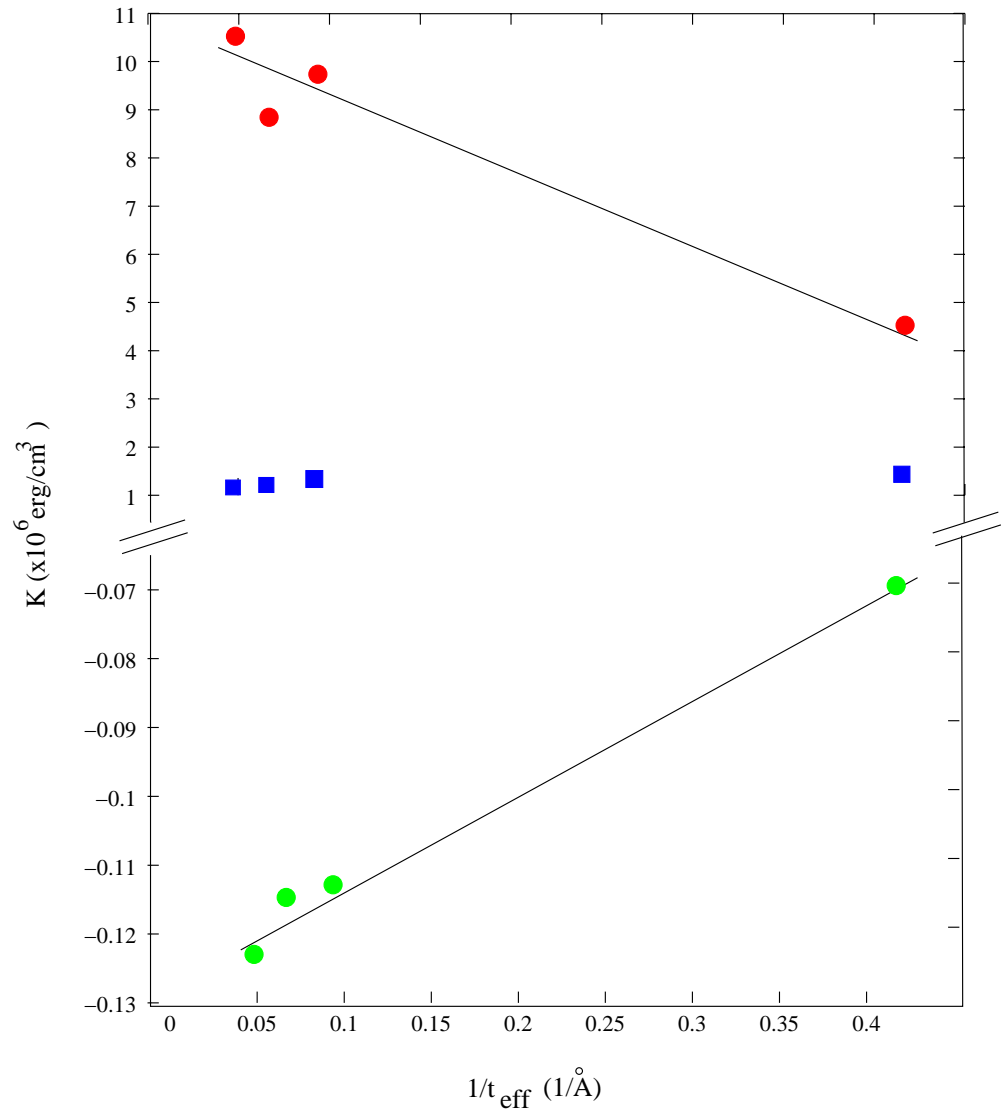


Figure 4.6: Anisotropy constants as a function of $1/t_{\text{eff}}$. The points are the actual data and the line is a linear fit. K_{U1} (blue), K_{U2} (green), and K (red) are shown.

Figure 4.7 shows the angle the AF moment makes with the applied field. Notice that when $H \perp c$ the AF moment is always $\perp H$. With $H \parallel c$ however, the AF moment rotates smoothly from $\parallel c$ at $H = 0$ to $\perp c$ at $H = 2\text{kOe}$. Above 2kOe the AF moment is $\perp H$ regardless of the field direction.

For a more detailed description we start by assuming the total moment per Co atom is $M_{tot} = 1.47\mu_B/\text{Co}$ and a homogeneous model. Equation 4.2 below is nothing more than an expression of the total neutron intensity at the AF peak,

$$|M_{tot}|^2 = |M_{AF\parallel}|^2 + |M_{AF\perp}|^2 + |M_F|^2, \quad (4.2)$$

where $M_{AF\parallel(\perp)}$ is the antiferromagnetic moment \parallel (\perp) H measured by the neutron experiment, and M_F is the ferromagnetic moment which was not measured directly, but derived from the values of $M_{AF\parallel}$ and $M_{AF\perp}$. Figure 4.8 shows $M_{AF\parallel}$, $M_{AF\perp}$ and M_F as a function of H . For $H \perp c$, a continuous transformation from $M_{AF\perp}$ at $H = 0$ to M_F as H increases is observed, as expected in a regular antiferromagnet. For the $H \parallel c$ case, the spin-flop transition between $M_{AF\parallel}$ and $M_{AF\perp}$ is gradual.

Shown in figure 4.9 is the vector magnetization in adjacent layers of Co as a function of H . In the $H \parallel c$ case the spin-flop transition is clearly seen. The neutron experiments show that the spin-flop transition is a second order phase transition, unlike traditional bulk antiferromagnets where the transition is first order. A first order transition would result in a sudden shift from $\phi = 0^\circ$ to $\phi = 90^\circ$ at a critical field, whereas we observe a gradual rotation of $\vec{M}_1 - \vec{M}_2$ as a function of field. One reason for this is that a surface SF transition occurs at a lower field, and then propagates through the sample toward the center of the sample as the field is increased [3]. Other possibilities are a slight misalignment between H and c , or interface disorder causing a distribution of coupling strengths throughout the sample.

To test the surface spin-flop theory discussed earlier in section 2.6.2, two samples

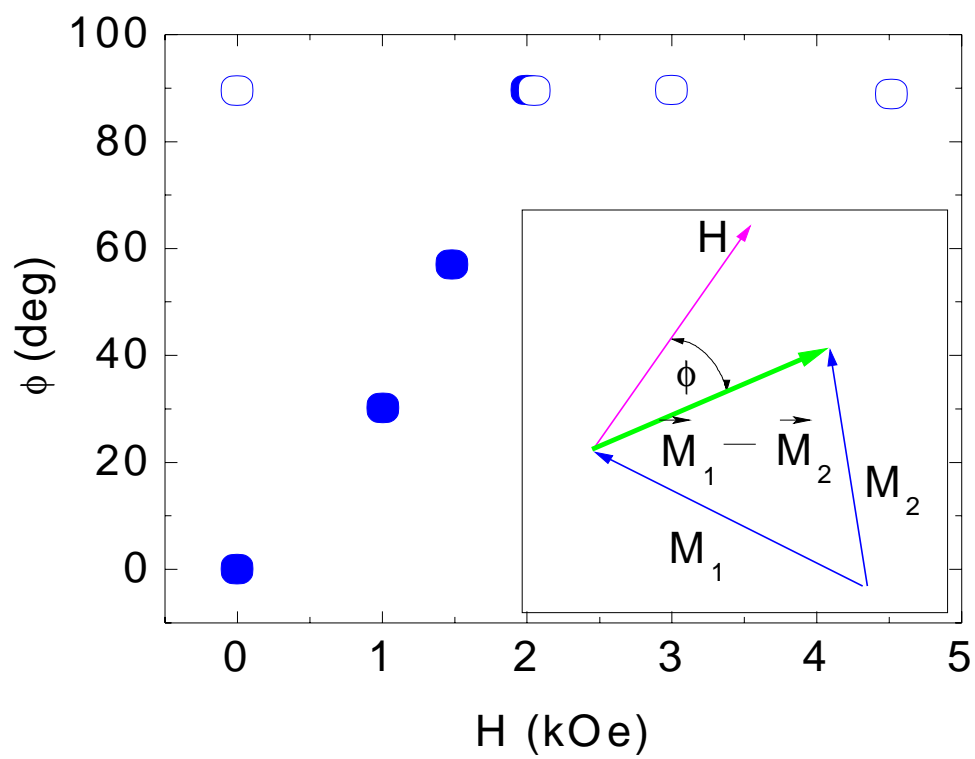


Figure 4.7: Angle between M_{AF} and c as a function of H . The ● are measured with $H \parallel c$ and ○ are measured with $H \perp c$.

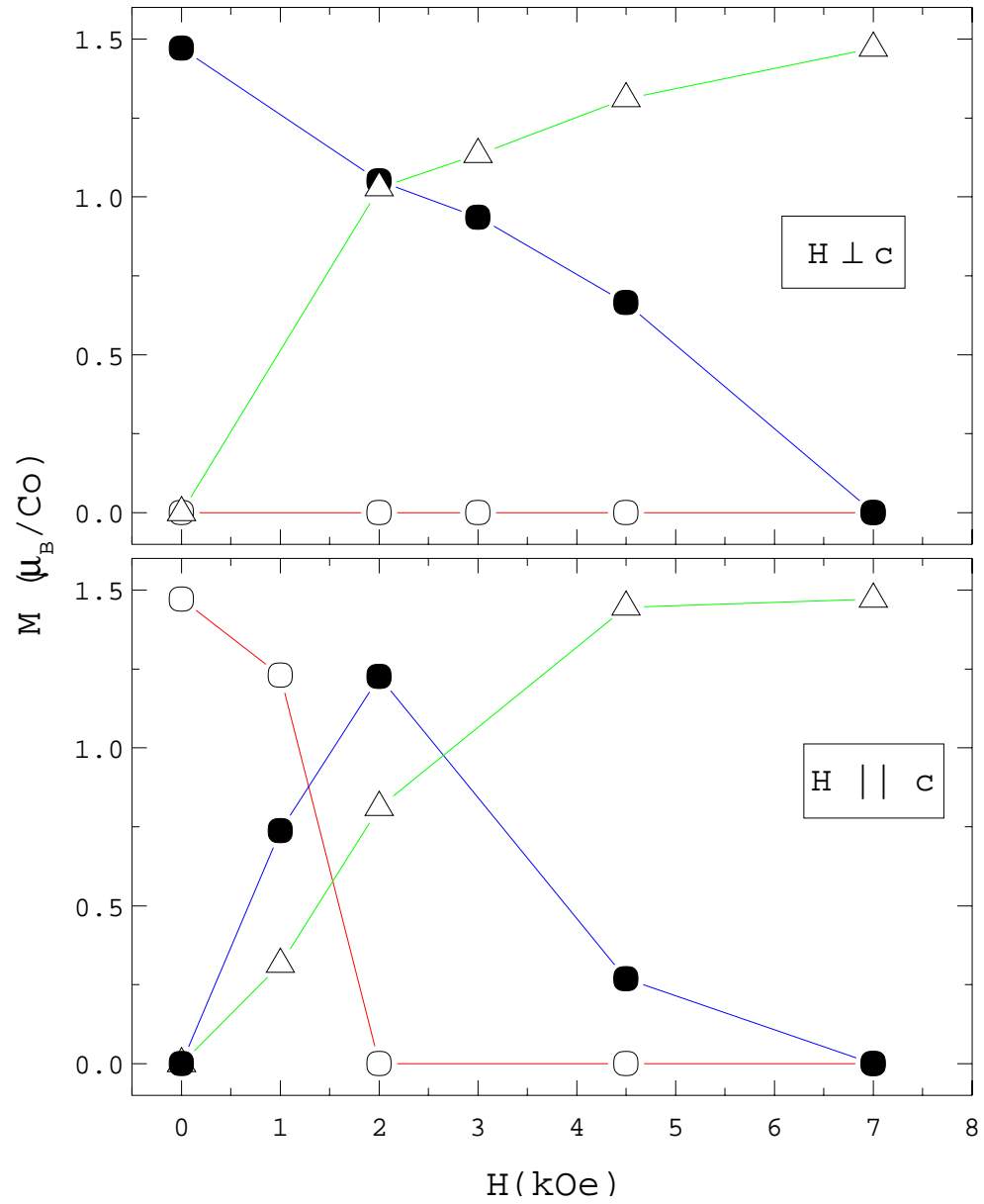


Figure 4.8: $M_{AF\perp}$ (●), $M_{AF\parallel}$ (○), and M_F (△) obtained from neutron diffraction with spin polarization analysis.

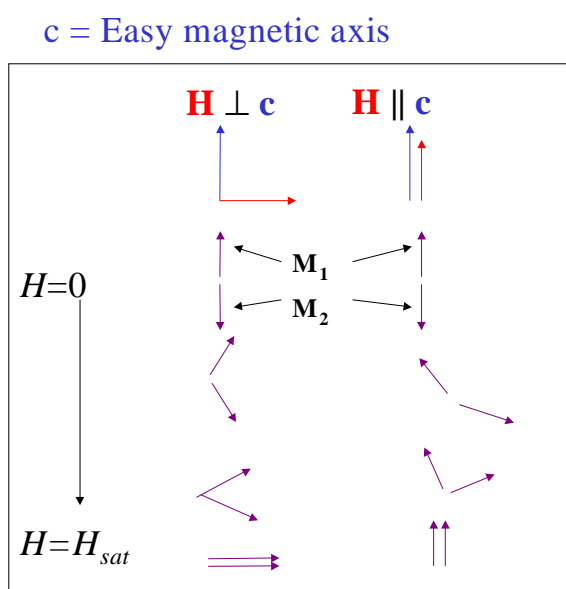


Figure 4.9: Schematic of the magnetization in adjacent layers of Co.

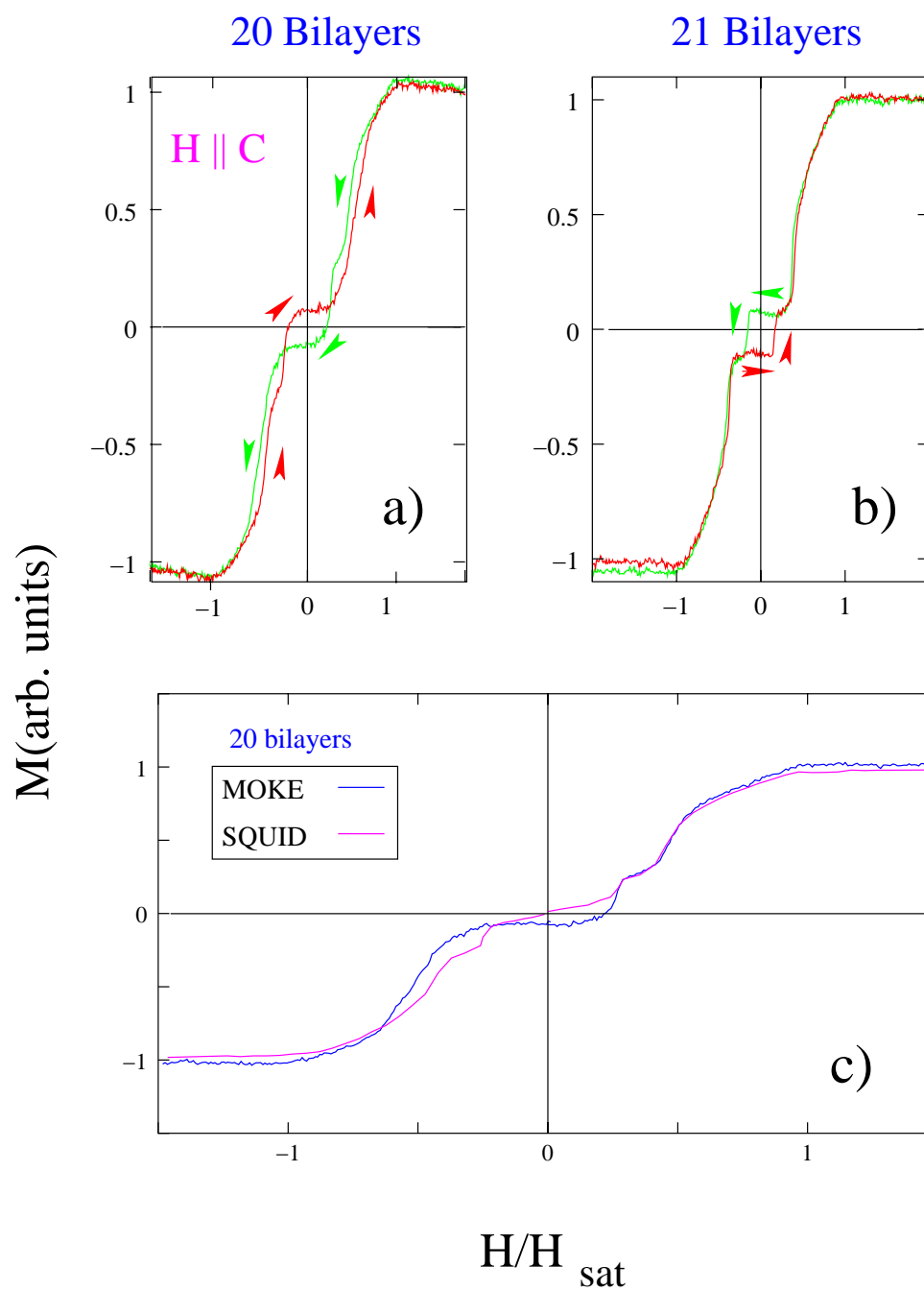


Figure 4.10: MOKE hysteresis loops for a superlattice with (a) 20 bilayers and (b) 21 bilayers. Color coding and arrows denote the sweep direction. (c) SQUID and MOKE magnetization curves from $+H_{sat}$ to $-H_{sat}$.

were grown at the same time, except that a mask was placed over one of them while an additional bilayer was grown on the other. Plotted in figure 4.10 (a) and (b) are the MOKE data for the 20 and 21 bilayer superlattices respectively. The MOKE experiment is surface sensitive and only measures the top five bilayers due to the limited skin-depth of the Co and Re metals for visible light. Starting at a positive saturation field and decreasing the field a domain wall forms in the center of the film. At $H/H_{sat} \sim 0.5$, according to the theory the domain wall completely encompasses the entire film thickness. This is the bulk spin flop field H_B described in 2.6.2. Up to this point the 20 and 21 bilayer samples behave similarly. Subsequently the magnetization in the odd sample drops sharply and levels prior to $H/H_{sat} = 0$, because the magnetization in the surface layer is pointing along the field direction. In the even sample, however, the change in slope between $H/H_{sat} = 0.5$ and $H/H_{sat} = 0.2$ corresponds to the motion of a domain wall toward the surface of the sample. Then a sharp drop in the magnetization to $M = 0$ occurs at $H/H_{sat} = H_{SSF} \sim 0.2$, where the domain wall is at the surface and the magnetization in the top two layers are normal to the field direction. Between $H/H_{sat} = 0.2$ and $H/H_{sat} = 0$ the magnetization is negative presumably because the top layer orients antiparallel to the field and the MOKE is surface sensitive. This is confirmed by the absence of the negative magnetization in the SQUID data (figure 4.10 (c)), where all layers are sensed equally. Notice the similarity with the theoretical calculations in figure 2.5. These experiments also support the view that the gradual change in ϕ observed by polarized neutron reflectivity is due to a surface spin-flop transition.

The surface spin-flop theory illustrated above and in section 2.6.2 requires $|J| \gg K$, or in units of magnetic field $|H_E| \gg H_A$, but what happens when this is no longer true? Figure 4.11(a) shows the hysteresis loops with $H \parallel c$ for an 18 bilayer superlattice where we believe J and K are comparable. The MOKE shows pronounced steps which presumably correspond to domain wall jumps as the domain wall moves inside the

sample, or the reversal of individual magnetic layers near the surface. The SQUID data, which is a measure of the whole sample, do not show sharp steps like the MOKE. Instead, they show a change in slope corresponding to each step in the MOKE in figure 4.11 (b). The resistivity data also have features similar to both the MOKE and SQUID loops. This sharp step evident at $H \sim 1$ kOe in the ρ data is caused by the formation of the domain wall near the center of the sample.

4.4 Spin-Dependent Scattering

By using the vector direction of the magnetization in adjacent layers of Co as a function of applied magnetic field given by the neutron experiments, an empirical model for the magnetoresistance can be built. The angular dependence of the AMR for one magnetic layer is found by rewriting equation 2.1 as

$$\rho_{AMR}(H) = \rho_{\parallel} \cos^2 \gamma(H) + \rho_{\perp} \sin^2 \gamma(H) \quad (4.3)$$

where $\cos \gamma(H) = \vec{M}(H) / |\vec{M}(H)| \cdot \vec{T} / |\vec{T}|$, $\rho_{\parallel(\perp)}$ is the resistivity with $\vec{M} \parallel (\perp) \vec{T}$, and \vec{T} is the current [20]. This can easily be extended to include two adjacent magnetic layers and normalized to the saturation value at high field. For the $H \parallel I$ geometry,

$$\begin{aligned} \frac{\rho_{AMR}(H) - \rho_{sat}}{\rho_{sat}} &= \frac{\rho_{AMR}(H) - \rho_{\parallel}}{\rho_{\parallel}} \quad (4.4) \\ &= \left(1 - \frac{1}{2} \cos^2 \gamma_1(H) - \frac{1}{2} \cos^2 \gamma_2(H) \right) \left(\frac{\rho_{\perp}}{\rho_{\parallel}} - 1 \right), \end{aligned}$$

and for $H \perp I$ geometry,

$$\begin{aligned} \frac{\rho_{AMR}(H) - \rho_{sat}}{\rho_{sat}} &= \frac{\rho_{AMR}(H) - \rho_{\perp}}{\rho_{\perp}} \quad (4.5) \\ &= \left(\frac{1}{2} \cos^2 \gamma_1(H) + \frac{1}{2} \cos^2 \gamma_2(H) \right) \left(\frac{\rho_{\parallel}}{\rho_{\perp}} - 1 \right), \end{aligned}$$

where ρ_{sat} is the resistivity at saturation, and γ_1 and γ_2 are the angles that the magnetization in adjacent Co layers make with the applied current. Phenomenologically the

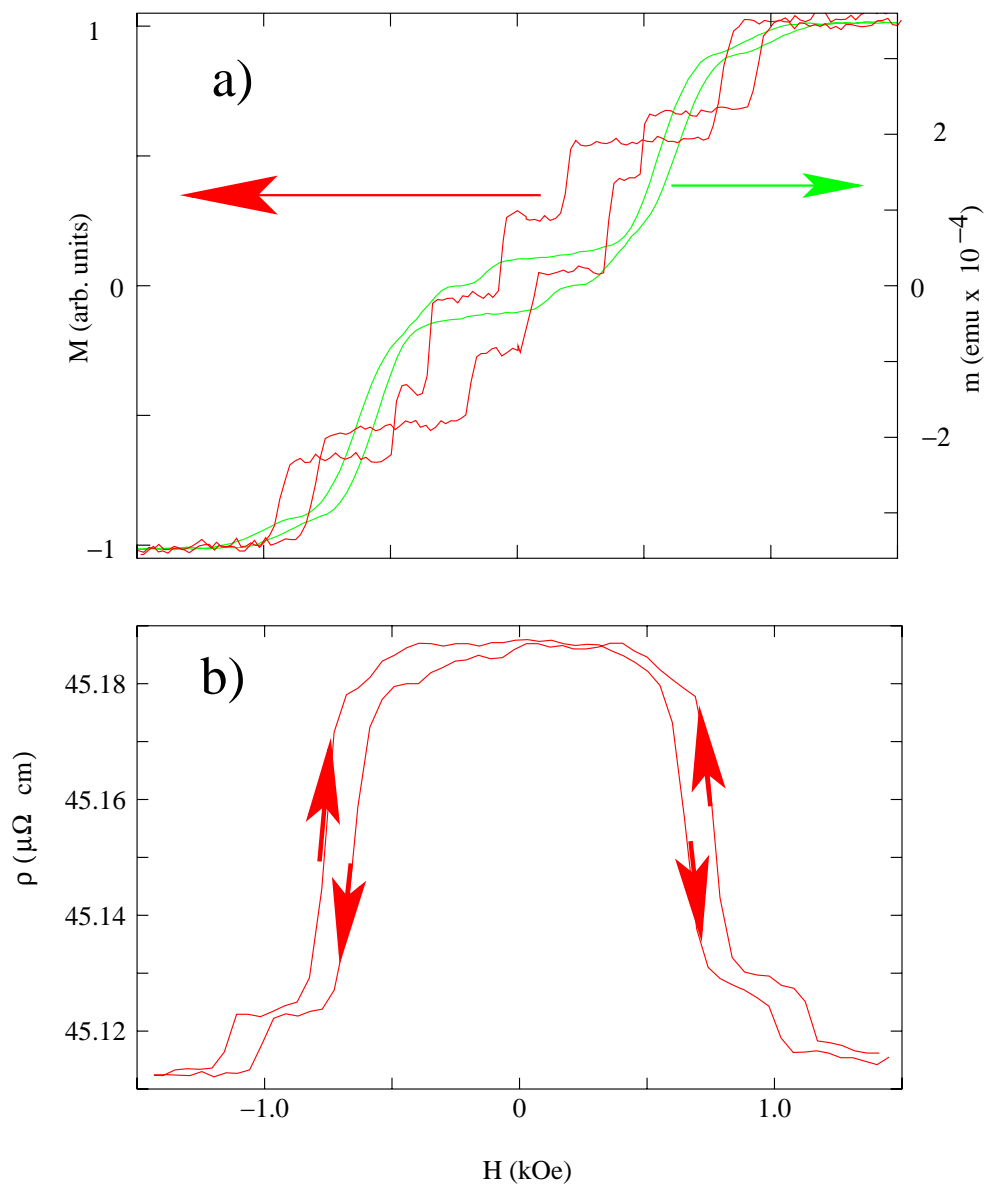


Figure 4.11: Hysteresis loops measured by MOKE and SQUID (a) and the resistivity (b) with $H \parallel c$ and $H \parallel I$ at $T = 300$ K.

GMR depends only on the antiferromagnetic alignment of the adjacent magnetic layers, so

$$\frac{\rho_{GMR}(H) - \rho_{sat}}{\rho_{sat}} = A \frac{|\vec{M}_1(H) - \vec{M}_2(H)|}{|\vec{M}_1(H=0) - \vec{M}_2(H=0)|}, \quad (4.6)$$

where \vec{M}_1 and \vec{M}_2 are the magnetizations in adjacent layers of cobalt as functions of applied magnetic field and A is a constant. \vec{M}_1 , \vec{M}_2 , γ_1 and γ_2 were experimentally determined from previous neutron reflectivity measurements performed at room temperature (see section 4.3). Notice that equation 4.6 implies a parallel resistor model where the spin-up and spin-down electrons scatter independently [19, 20], and that magnetic layers polarize the conduction electrons. Equations 4.4 and 4.5 assume a parallel resistor model that includes a spin-orbit interaction, which causes the $s - d$ scattering to be anisotropic [19]. This anisotropic $s - d$ scattering is the standard explanation of the existence of AMR in bulk ferromagnets(see section 2.4.1).

In figure 4.12 the MR dips at $H = 1.5$ kOe in the $H \parallel c / H \parallel I$ geometry and dips at $H = 0$ kOe in the $H \parallel c / H \perp I$ geometry at high temperatures. The MR also evolves differently as a function of temperature. Since the dips in the MR remain at approximately the same field at all temperatures, one can assume the magnetizations $\vec{M}_1(H)$ and $\vec{M}_2(H)$ do not significantly depend on temperature. This leaves all of the temperature dependence in the coefficient A and the ratio $(\rho_{\perp}/\rho_{\parallel})$. By simulating the $MR = AMR + GMR$ with the above equations, and using A and resistivity ratio $(\rho_{\perp}/\rho_{\parallel})$ as adjustable parameters, the data are qualitatively reproduced as shown in figure 4.13 for the 5 K data set. Our simple empirical model, relying on \vec{M}_1 and \vec{M}_2 as a function of H determined from the neutron reflectivity, does not take into account possible domain formation in the Co layers, which could alter the magnetoresistance [56]. This could explain why the model reproduces the qualitative features of the data, such as the dips near $H = 0$, but not the exact quantitative experimental results.

Only one physical constraint was placed on the adjustable parameters in the sim-

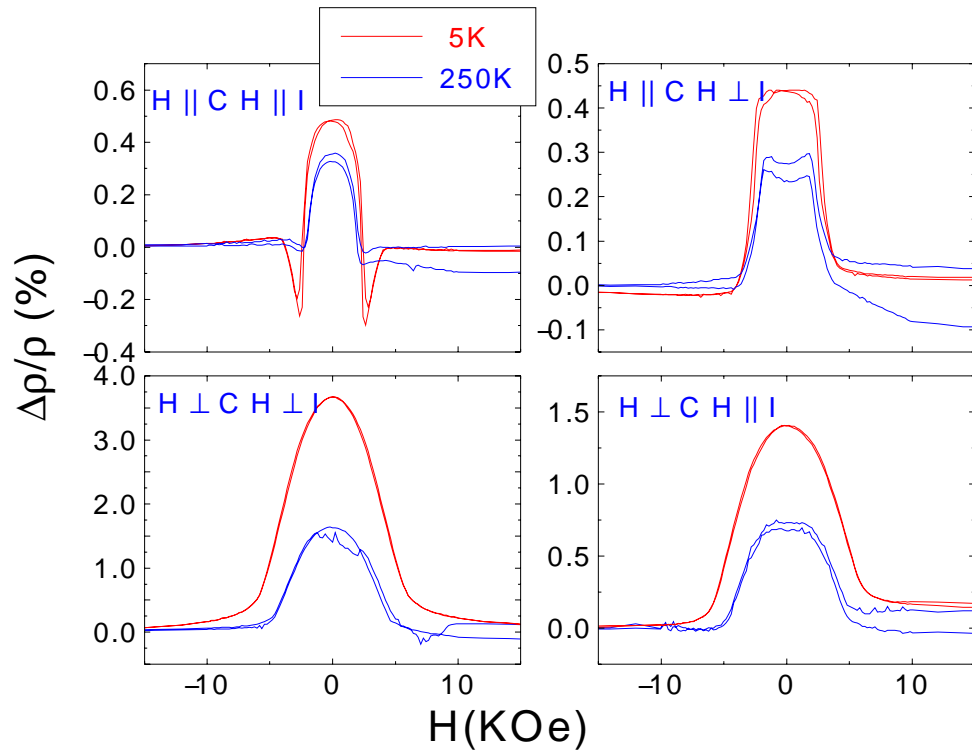


Figure 4.12: The magnetoresistance as a function of magnetic field at $T = 5$ K (red) and $T = 250$ K (blue) for four separate geometries. The data were obtained measuring from positive to negative and negative to positive fields. The difference in the values at high positive fields are due to small differences in the temperature.

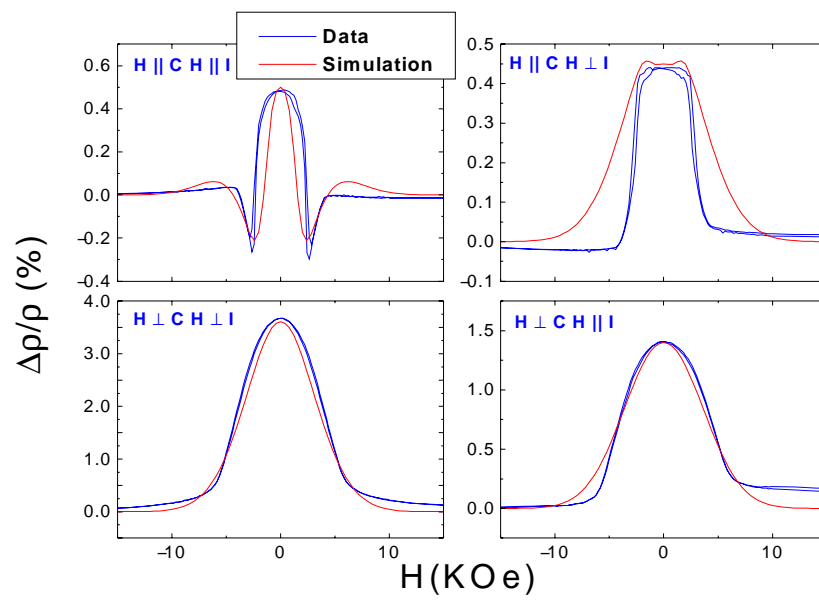


Figure 4.13: Magnetoresistance measurements (blue) and simulation (red) at $T = 5$ K. The simulation qualitatively matches the data.

ulation: that the ratio ($\rho_{\perp}/\rho_{\parallel}$) must be the same for the current flowing along a given crystallographic direction. This is reasonable because $\rho_{\perp}/\rho_{\parallel}$ is proportional to the ratio of the spin up and spin down resistivities, which only depends on the crystallographic direction in which the current is flowing [19, 20]. Figure 4.14 shows the simulation broken down into its AMR and GMR components. Notice that the interesting dips in the MR are only due to the AMR contribution. One theoretical explanation for the existence of GMR in multilayers is the matching of the band structure of the non-magnetic layer with the spin-up or spin-down bands in the magnetic layer [57]. The small GMR of Co/Ir superlattices has been blamed on the lack of band matching of the Ir with the Co spin-up or spin-down bands [12]. In Co/Re, the Re bands are similar to the spin-down bands of Co. This means that the GMR in Co/Re should be large, but we only measure a GMR of 2.5% at 5 K. The low value can be explained by the relatively few electrons that traverse the Re spacer to the next Co-Re interface without being scattered. Future measurements with the current perpendicular to the plane should test this hypothesis.

Figure 4.15(a) shows that the temperature dependence of the AMR depends on which crystallographic direction the sensing current flows. The GMR is usually considered to be isotropic, but figure 4.15(b) shows that it is anisotropic in both current and field directions. Other authors have also found the GMR to be anisotropic and dependent on the asymmetry in the spin-dependent resistivity ratio ($\rho_{\uparrow}/\rho_{\downarrow}$) parallel and perpendicular to the current. As a reminder from previous sections, AMR is a bulk effect relying on the electrons flowing through a ferromagnetic layer while in GMR both interface and bulk scattering may be important. By comparing the GMR to the AMR (figure 4.16), the nature of the scattering in GMR can be compared to the scattering in AMR. Since AMR results from scattering within the FM layer, any differences between the AMR and GMR must be due to the differences in the scattering mechanism responsible for the two effects. When $I \parallel c$ the curve is flat, indicating that the

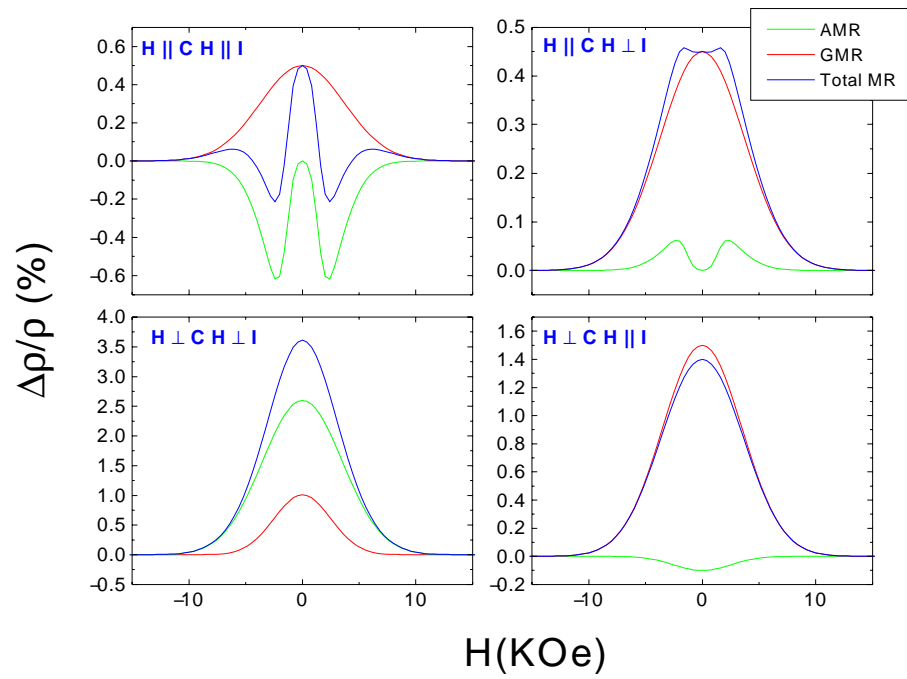


Figure 4.14: Simulation broken down into total MR (blue), AMR (green) and GMR (red) contributions.

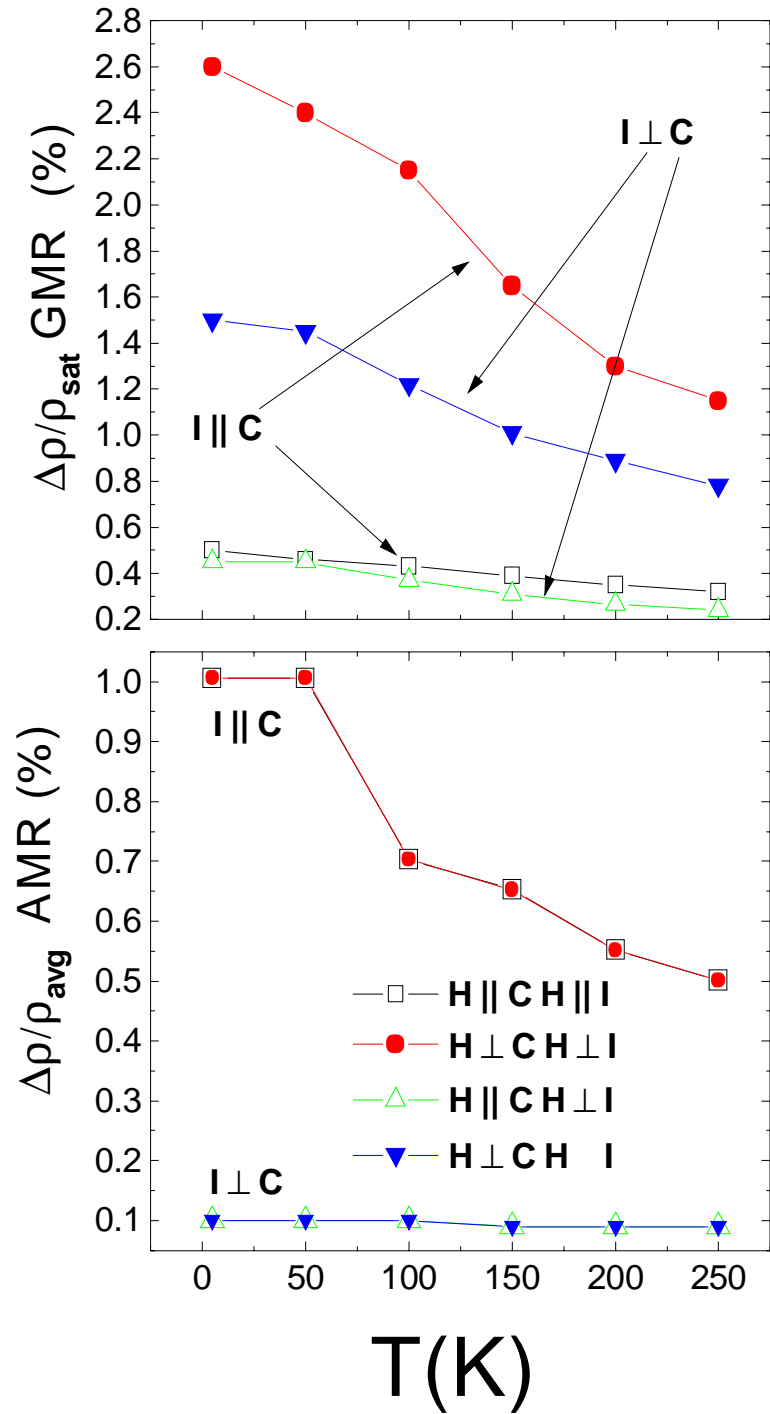


Figure 4.15: Magnitude of the AMR and the GMR plotted as a function of temperature.

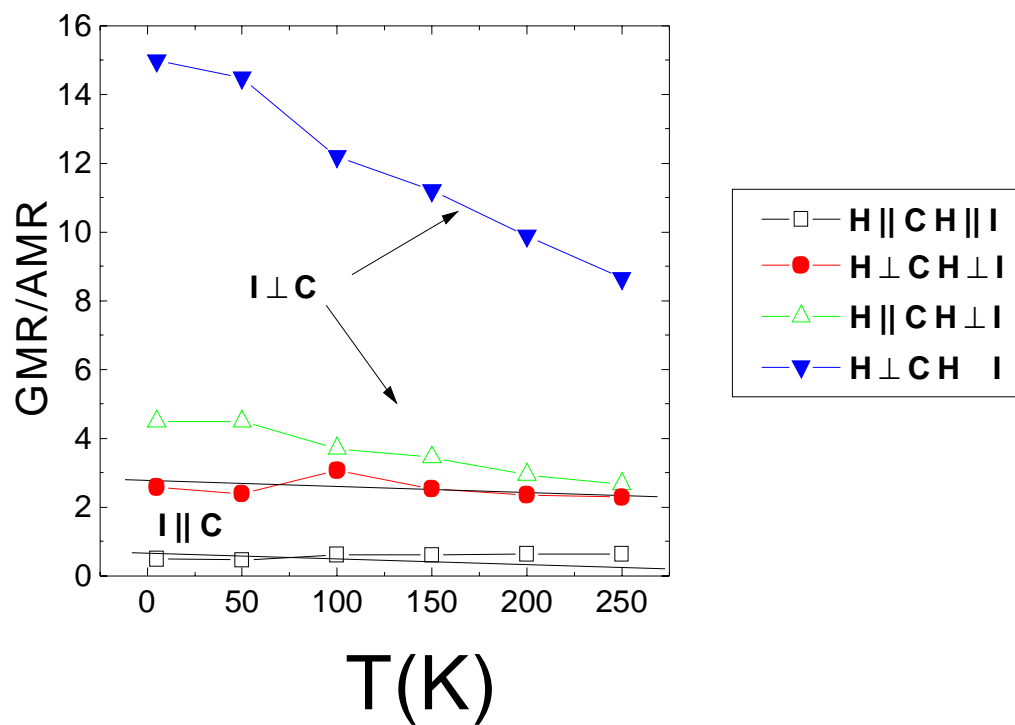


Figure 4.16: The magnitude of GMR/AMR plotted as a function of temperature.

AMR and the GMR have a similar temperature dependence. This suggests that when $I \parallel c$ bulk scattering is important to GMR. In the other case, $I \perp c$, the curves in figure 4.16 are not flat, indicating that the temperature dependence of the AMR and the GMR is different, meaning that for $I \perp c$, interface scattering is more important. This is not entirely surprising since the c -axis represents a strong crystallographic anisotropy, which leads to an anisotropic Fermi surface in the plane of the sample. This is confirmed by figure 4.17, which shows the magnitude of the resistivity of the sample with $I \parallel c$ and $I \perp c$. This agrees with the measurements in pure Co single crystals, where $\rho_{I \parallel c} > \rho_{I \perp c}$ [16]. Hence, the two important findings from these experiments are that 1) the GMR is in general anisotropic because of asymmetries in the Fermi surface; and 2) the spin-dependent scattering responsible for GMR can occur preferentially either at the interface or in the bulk of the ferromagnetic layers depending on how the current is applied. Noting that $\rho_{I \parallel c} > \rho_{I \perp c}$, the latter finding makes sense because the electron mean free path strongly depends on the direction in which the current is applied.

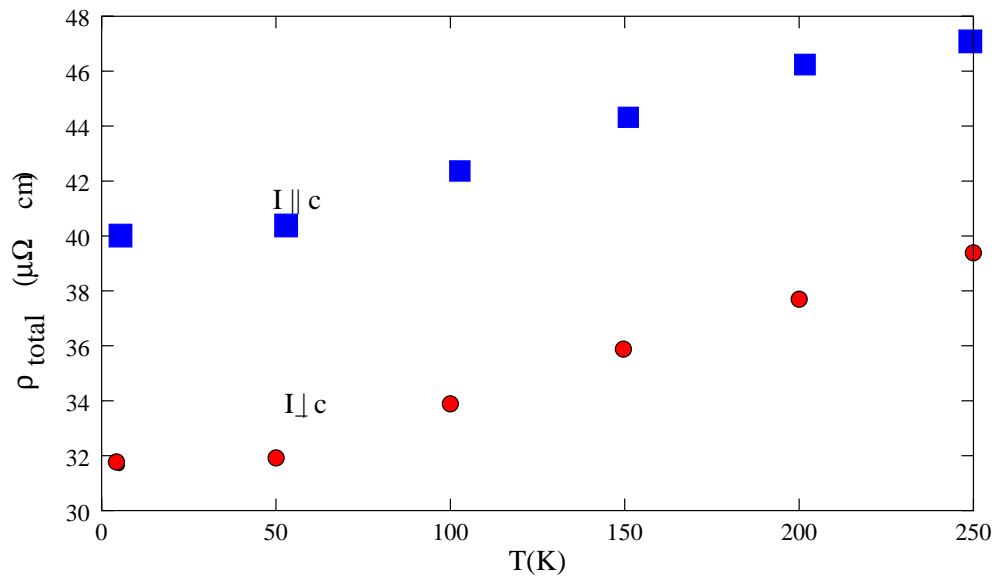


Figure 4.17: Resistivity as a function of temperature at $H = 0$.

Chapter 5

Conclusions

Using Co/Re superlattices we made several important discoveries. 1) Magnetization measurements in antiferromagnetically-coupled samples agree with surface spin-flop transition theory and previous measurements [3]. 2) This shows that the theory is universal and applies to systems other than just Fe/Cr. FMR studies have found a small out-of-plane interface induced anisotropy. To our knowledge this is the first evidence of an out-of-plane anisotropy in a system with the Co hcp c -axis in the film plane. 3) By combining neutron reflectivity and MR studies we were able to simulate the MR of a superlattice. The simulations showed that the AMR and GMR contributions could be identified. Like other authors [58] we also found that the GMR is anisotropic. By comparing the magnitude of the AMR to the GMR as a function of temperature, the GMR was found to behave like a bulk scattering effect in some geometries and an interface effect in others.

There is still work to be done with Co/Re superlattices. For instance, more polarized neutron reflectivity studies will give the magnetization direction as a function of both field and depth in the sample. This is needed to refine our electron transport model. Measurements of the magnetotransport in current perpendicular to the plane (CPP) geometry should also be carried out because the interpretation of the GMR would be simpler. In addition, the effect of a large Re layer resistance would be minimized.

Bibliography

- [1] A. R. Miedem and J. W. F. Dorleijn, Philips Technical Review **35**, 29 (1975).
- [2] S. Chikazumi, Physics of Magnetism (Wiley, New York, 1964), pp. 419-421.
- [3] R. W. Wang, D. L. Mills, E. E. Fullerton, J. E. Mattson, and S. D. Bader, Phys. Rev. Lett. **72**, 920 (1994).
- [4] U.S. Inc. Sputtering Source Manual **1**, 1 (1989).
- [5] Y. D. Yao, Y. Liou, J. C. A. Huang, S. Y. Liao, I. Klik, W. T. Yang, C. P. Chang, and C. K. Lo, J. Appl. Phys. **79**, 6533 (1990).
- [6] E. E. Fullerton, M. J. Conover, J. E. Mattson, C. H. Sowers, and S. D. Bader, Phys. Rev. B **48**, 15 755 (1993).
- [7] A. Dina and K. Ounadjela, J. Magn. Magn. Mater. **146**, 66 (1995).
- [8] B. H. Miller, E. Y. Chen, and E. D. Dahlberg, J. Appl. Phys. **79**, 6384 (1993).
- [9] J. S. Jiang, A. Inomata, C. Y. You, J. E. Pearson, and S. D. Bader, J. Appl. Phys. **89**, 6817 (2001).
- [10] A. Scheyer, C. F. Majkrzak, T. Zeidler, T. Schmitte, P. Bödeker, K. Theis-Bröhl, A. Abromeit, J. A. Dura, and T. Watanabe, Phys. Rev. Lett. **79**, 4914 (1997).
- [11] A. Fert, P. Grünberg, A. Barthélémy, F. Petroff, and W. Zinn, J. Magn. Magn. Mater. **140-144**, 1 (1995).
- [12] H. Yanagihara, K. Pettit, M. B. Salamon, E. Kita, and S. S. P. Parkin, J. Appl. Phys. **79**, 6370 (1997).
- [13] Y. Luo, B. Pfeifer, A. Kaeufler, M. Moske, and K. Samwer, J. Appl. Phys. **87**, 2479 (2000).
- [14] H. Yanagihara, E. Kita, and M. B. Salamon, Phys. Rev. B **60**, 12 957 (1999).
- [15] D. L. Mills, Phys. Rev. Lett. **20**, 18 (1968).

- [16] S. V. Vonsovskii, Magnetism (Wiley and Sons, New York, 1974), Vol. 1, pp. 5–10, 121.
- [17] R. A. Serway, Physics for Scientist and Engineers (Saunders College Publishing, Philadelphia, 1990).
- [18] C. Kittel, Introduction to Solid State Physics (Wiley and Son, New York, 1996).
- [19] T. R. McGuire and R. I. Potter, *IEEE Trans. Magn.* **11**, 1018 (1975).
- [20] I. A. Campbell and A. Fert, Ferromagnetic Materials (North-Holland, Amsterdam, 1982), Vol. 3, p. 775.
- [21] K. J. Eijkel and J. H. Fluitman, *IEEE Trans. Mag.* **MAG-22**, 955 (1986).
- [22] J. Smit, *Physica* **14**, 621 (1951).
- [23] L. Berger, *Physica* **38**, 1083 (1965).
- [24] M. N. Baibich, J. M. Broto, A. Fert, F. Nguyen Van Dau, F. Petroff, P. Eitenne, G. Creuzet, A. Friedrich, and J. Chazelas, *Phys. Rev. Lett.* **61**, 2472 (1988).
- [25] P. Grünberg, R. Schreiber, Y. Pang, M. B. Brodsky, and H. Sowers, *Phys. Rev. Lett.* **57**, 2495 (1986).
- [26] S. S. P. Parkin, N. More, and K. P. Roche, *Phys. Rev. Lett.* **64**, 2304 (1990).
- [27] E. E. Fullerton, D. M. Kelly, J. Guimpel, and I. K. Schuller, *Phys. Rev. Lett.* **68**, 859 (1992).
- [28] S. S. P. Parkin, *Phys. Rev. Lett.* **71**, 1641 (1993).
- [29] L. V. Melo, P. Monteiro, and P. P. Freitas, *J. Magn. Magn. Mater.* **121**, 290 (1993).
- [30] B. Dieny, *J. Magn. Magn. Mater.* **136**, 335 (1994).
- [31] B. H. Miller, B. P. Stojković, and E. D. Dahlberg, *Phys. Lett. A* **256**, 294 (1999).
- [32] P. P. Freitas, L. V. Melo, I. Trindade, M. From, J. Ferreira, and P. Monteiro, *Phys. Rev. B* **45**, 2495 (1992).
- [33] J. R. Christman, Fundamentals of Solid State Physics (Wiley and Sons, New York, 1988).
- [34] L. Néel, *Ann. Phys. (Paris)* **5**, 232 (1936).
- [35] N. J. Poulis and G. E. G. Hardeman, *Physica (Utrecht)* **18**, 201 (1952).
- [36] F. Keffer and H. Chow, *Phys. Rev. Lett.* **31**, 1061 (1973).

- [37] E. E. Fullerton, M. J. Conover, J. E. Mattson, C. H. Sowers, and S. D. Bader, *Phys. Rev. B* **48**, 1794 (1993).
- [38] S. K. Sinha, E. Sirota, S. Garoff, and H. B. Stanley, *Phys. Rev. B* **38**, 2297 (1988).
- [39] B. Vidal and P. Vincent, *Appl. Opt.* **23**, 1794 (1984).
- [40] W. H. Press, S. A. Teukolsky, W. T. Vetterling, and B. P. Flannery, *Numerical Recipes in C: The Art of Scientific Computing* (Cambridge University Press, Cambridge, 1992).
- [41] M. A. Thomaz, G. R. Harp, E. Mayo, D. Lederman, R. Wu, and W. L. O'Brien, *J. Vac. Sci. Technol. A* **16**, 1336 (1998).
- [42] M. M. Schwickett, R. Coehoorn, M. A. Tomaz, E. Mayo, D. Lederman, W. L. O'Brien, T. Lin, and G. R. Harp, *Phys. Rev. B* **57**, 13 681 (1998).
- [43] E. E. Fullerton, I. K. Schuller, H. Vanderstraeten, and Y. Bruynseraede, *Phys. Rev. B* **45**, 9292 (1992).
- [44] Y. Huai, R. W. Cochrane, and M. Sutton, *Phys. Rev. B* **48**, 2568 (1993).
- [45] L. V.Melo, I. Trindade, M. From, P. P. Freitas, N. Teixeira, M. F. da Silva, and J. C. Soares, *J. Appl. Phys.* **70**, 7370 (1991).
- [46] S. D. Bader, *J. Magn. Magn. Mater.* **100**, 440 (1991).
- [47] W. G. Jenks, I. M. Thomas, and J. P. Wikswo, *Encyclopedia of Applied Physics* **19**, 457 (1997).
- [48] F. Schreiber, Z.Frait, T. Zeidler, N. Metoki, W. Donner, H. Zabel, and J. Plezl, *Phys. Rev. B* **51**, 2920 (1995).
- [49] G. P. Felcher, R. O. Hilleke, R. K. Crawford, J. Haumann, and G. Ostrowski, *Rev. Sci. Instr.* **58**, 609 (1987).
- [50] L. J. van der Pauw, *Philips Research Report* **13**, R334 (1958).
- [51] J. Z. Hilt, J. J. Picconatto, A. O'Brien, M. J. Pechan, and E. E. Fullerton, *J. Mang. Magn. Matter.* **198-199**, 387 (1999).
- [52] M. Grimsditch, E. E. Fullerton, and R. L. Stamps, *Phys. Rev. B* **56**, 2617 (1997).
- [53] S. S. P. Parkin, N. More, and Roche, *Phys. Rev. Lett.* **64**, 3204 (1990).
- [54] K. Hyomi, A. Murayama, J. Eickmann, and C. M. Falco, *J. Magn. Magn. Mat.* **198-199**, 378 (1999).
- [55] T. Zeidler, K. Theis-Bröhl, and H. Zabel, *J. Magn. Magn. Mater.* **187**, 1 (1998).

- [56] W. Folkerts, J. Magn. Mater. **94**, 302 (1991).
- [57] W. H. Butler, X. G. Zhang, D. M. C. Nicholson, and J. M. MacLaren, J. Magn. Mater. **151**, 354 (1995).
- [58] B. Dieny, C. Cowache, A. Nossou, P. Dauguet, J. Chaussy, and P. Gandit, J. Appl. Phys. **79**, 6370 (1996).

Timothy Charlton

Education

Ph. D. Physics	West Virginia University, 2001
B. S. Physics	West Virginia University, 1996

Employment

Research Assistant	West Virginia University, 1997 - 2001
Teaching Assistant	West Virginia University, 1996 - 1998
Undergraduate	West Virginia University, 1994, 1996
Research Assistant	

Awards and Honors

Outstanding Teaching Assistant in Physics, 1997 - 1998

Professional Activities

Referee	Journal of Applied Physics
Memberships	American Physical Society, Materials Research Society